High accuracy attitude determination of a spacecraft with a fast-rotating Doppler radar reflector

Acta Astronautica 233 (2025) 66–81

Contents lists available at ScienceDirect

Acta Astronautica

journal homepage: www.elsevier.com/locate/actaastro

Research paper

High accuracy attitude determination of a spacecraft with a fast-rotating Doppler radar reflector

Francesco Manconi [a,b,*], Paolo Martire [a,b], Fabrizio Stesina [a], Alessandro Battaglia [b]

[a] Department of Mechanical and Aerospace Engineering, Politecnico di Torino, Corso Duca degli Abruzzi 24, 10129, Turin, Italy
[b] Department of Environment, Land and Infrastructure Engineering, Politecnico di Torino, Corso Duca degli Abruzzi 24, 10129, Turin, Italy

ARTICLE INFO

Keywords:
Spacecraft dynamics
Attitude determination
Kalman filter
Doppler radar
Rotating antenna

ABSTRACT

The attitude dynamics of a spacecraft employing a large rotating appendage is complex, and control and determination of its attitude and pointing can be a real challenge considering the impact system uncertainties and sensor errors can have on the mission scientific products. The aim of this paper is to develop a multi-rigid-body model that describes the rotational motion of an Earth-observing scientific satellite equipped with a large conically-scanning antenna reflector. The antenna assembly is statically and dynamically balanced, and a Sliding Mode Controller is implemented for achieving the desired attitude and angular velocity. Then, the determination problem is addressed, in order to verify the system capabilities in guaranteeing the mission knowledge requirements through simulations. A full suite of sensor feeds measurements to an Extended Kalman Filter algorithm running a simplified model of the spacecraft dynamics, and the spacecraft attitude and antenna pointing are estimated. The spacecraft configuration and operational conditions are based on the WIVERN mission, currently under study at ESA, which aims at characterizing global winds via a Doppler radar fast-rotating antenna. In particular, the velocity component of the spacecraft along the antenna line-of-sight is taken into consideration, as errors in the determination of this quantity directly influence the quality of the observed wind speed. It is demonstrated that the determination system can achieve an Absolute Knowledge Error (AKE) under 100 μrad per axis in terms of attitude, and under 1 m/s in terms of line-of-sight (LOS) velocity error. Spectral analysis shows that the filter lowers high frequency contributions to the AKE, which is a desired outcome as lower frequency errors can be corrected in post-processing using data-driven calibration methods. Criticalities regarding antenna unbalance and star tracker bias uncertainties are discussed by means of worst-case scenarios simulations and Monte Carlo campaigns.

1. Introduction

Recent years have witnessed a growing interest in Earth Observation space missions that employ scanning sensors with large swath, thus enabling much shorter revisit times. Microwave sensor payloads are often required to penetrate clouds and precipitation in the Earth's atmosphere. However, the use of microwave wavelengths requires missions in LEO and large antennas to achieve fine spatial resolutions (on the order of a few kilometres or better), which are essential to map the spatial variability of atmospheric observables such as wind, clouds and precipitation, or surface properties such as currents or sea ice cover. Examples of such missions featuring large spinning reflectors as payload, are the NASA's Global Precipitation Measurement Microwave Imager [1] and Soil Moisture Active Passive (SMAP) missions [2], as well as ESA's Copernicus Imaging Microwave Radiometer (CIMR) [3] mission.

Of particular interest in this category are future active (radar) missions with large antennas and Doppler capabilities. The challenge is that the fast motion of the platform (of several km/s) makes the antenna pointing requirements extremely demanding, especially when the target velocity measurements must reach accuracies of the order of a few m/s (as for atmospheric winds) or a few cm/s (as for ocean currents). [4,5] has proposed a Ka-band pencil-beam Doppler scatterometer capable of mapping ocean winds and currents globally; this system is currently under investigation by NASA. Similarly, the WIVERN mission (www.WIVERN.polito.it, [6,7]) – short for WInd VElocity Radar Nephoscope – is now in Phase A as part of the ESA Earth

* Corresponding author at: Department of Environment, Land and Infrastructure Engineering, Politecnico di Torino, Corso Duca degli Abruzzi 24, 10129, Turin, Italy.
E-mail addresses: francesco.manconi@polito.it (F. Manconi), paolo.martire@polito.it (P. Martire), fabrizio.stesina@polito.it (F. Stesina), alessandro.battaglia@polito.it (A. Battaglia).

https://doi.org/10.1016/j.actaastro.2025.03.026
Received 23 December 2024; Received in revised form 7 March 2025; Accepted 22 March 2025
Available online 3 April 2025

Explorer 11 program. The observational approach of WIVERN is based on Doppler signals acquired at different azimuth angles from a fast-rotating conically-scanning antenna [6,8]. If launched, the WIVERN Doppler radar is expected to provide the first measurements of winds within clouds and precipitation, including extreme weather events like tropical cyclones [9], thus filling the gap in global observations of wind in cloudy regions.

For missions of this kind, one of the major needs is the attitude determination of the satellite and the payload, especially when an inaccurate knowledge of the instrument pointing affects the quality of the measurements, e.g. the Doppler velocities. This results in strict pointing Absolute Knowledge Error (AKE) requirements. For instance, the SKIM mission concept involves a rotating off-nadir beam with the aim of measuring ocean currents and waves using a Doppler radar [10]. Pointing knowledge requirements are stringent, with an RMS accuracy of 0.1 m/s or 0.001 deg at 12 deg incidence angle as observe phenomena are in the order of maximum 1 m/s. Similarly, for the ODYSEA mission concept, which aims at measuring sea surface winds and currents by means of a conically scanning Doppler scatterometer, a knowledge random error of 0.5 m/s for currents and 1 m/s for winds is recommended [11]. For the SMAP spacecraft, instead, the total allocated knowledge error budget for the attitude determination system is 0.015 deg per axis, which in terms of line-of sight velocity translates to roughly 1.6 m/s [2,12]. In summary, for multibody spacecraft with large rotating antennas, the determination problem is critical, with requirements that are specific to the observing system and also dependent on the timescale of observations.

The problem of simulation of the attitude determination and control of a multibody spacecraft is not a new one, but the application presents novel challenges, and the verification of the system capability in this context is necessary. For the SMAP mission, a complex spacecraft model was examined [13]: a Model Predictive Control approach was used to counteract the perturbations caused by the large flexible spinning reflector. In [14], an attitude Sliding Mode Control was adopted to counteract disturbances caused by residual imbalances on the spinning rotor. A spacecraft with a large rotating payload with and Active Balancing System was studied in [15,16]. Expanding on these studies, an attitude determination system can be considered. An example can be found in [17], where an Unscented Kalman Filter (UKF) based iterative controller for a multibody rotating payload was proposed, combining the needs of a high-precision attitude determination and an accurate control of the rotation. In [18,19], modeling and simulation of a multibody satellite with a gimballed solar panel were performed, adopting a feedback linearization control and an UKF algorithm for determination. While in this case the application and focus differ from ours, the problem and its formulation are nevertheless highly relevant to our study.

The work presented in this paper focuses mainly on the rotating payload of the WIVERN mission and the verification of its scientific aims, by means of mathematical simulation. A solution is proposed for a large satellite equipped with an antenna operating in a conical scanning mode. The high rate of the rotation of the antenna and the classical errors and uncertainties of the sensors and actuators get more complicated having a high accuracy. The solution is based on a fast Extended Kalman Filter (EKF), which utilizes high-precision measurements from a star tracker with three optical heads for the satellite attitude, a tri-axial gyroscope for the direct measurement of the angular rate of the satellite, and an encoder measuring the angular motion of the antenna. The EKF fuses these measurements and merges them with the prediction part based on the simplified model of the system kinematics and dynamics with inputs coming from a Sliding Mode Controller (SMC). The robustness of the solutions on some system uncertainties is addressed with Monte Carlo simulation campaigns.

The proposed solution is verified on the data and requirements of the WIVERN mission which is characterized by a very large (3 m diameter parabolic antenna) spinning at about 12 rpm. WIVERN science requirements include knowledge of the antenna pointing better than 100 μrad in azimuth and elevation [7,20] and high-precision antenna pointing (i.e., Absolute Performance Error on the antenna boresight smaller than 1000 μrad). In terms of velocity along the antenna boresight, the AKE shall be lower than 1 m/s in absolute value.

A brief description of the article structure is provided. Section 2 presents the mathematical formulation of the problem, addressing the simulator architecture, the spacecraft multibody geometry, the derivation of the equations of motion and formulation of the control algorithm. Section 3 delves deeper into the determination system of the simulator, dealing with the sensor models and Kalman Filter implementation. In Section 4 simulation results are presented and discussed, addressing the satisfaction of mission requirements and criticalities specific to the case at hand. Conclusions are drawn in Section 5.

2. Problem formulation

In Fig. 1 a schematic of the simulation architecture is shown, with the various building blocks explained in the following paragraphs.

The *Plant* block represent the spacecraft model in terms of equations of motion; the *Control* block considers the control algorithm and actuators for pointing the spacecraft in the desired direction; the *Determination* block contains sensors and the filter algorithm for observing the system attitude; the *LOS Velocity* block takes as inputs the outputs of the determination and the true system state, producing the main outputs of the simulator in term of science goals, i.e. the knowledge error of the projection of the satellite velocity along the boresight direction.

2.1. Spacecraft model

Fig. 2 illustrates a schematic representation of the WIVERN spacecraft. The spacecraft layout consists of a set of individual bodies, each one labeled by a progressive number. All bodies are assumed rigid, meaning that their geometry does not change in time with respect to a reference frame fixed with each individual body. Nevertheless, relative rotations about fixed axes are permitted (i.e., rotors are allowed to rotate around their rotation axis).

The main body of the spacecraft, labeled as 1, is modeled as a hollow parallelepiped. An assembly of reaction wheels, labeled from 2 to 6, is embedded within the main body in a pyramidal configuration. While reaction wheels 2, 3, 4 and 5 are used to control the spacecraft attitude, reaction wheel 6 is devoted to the compensation of the antenna assembly angular momentum. All wheels are assumed to be statically and dynamically imbalanced to account for jitter perturbations (Fig. 3). The parabolic reflector, labeled as 8, is fitted to a rotating shaft connected to body 1 through the hinge point O^A. The balancing mass 7 is a sphere attached to the same shaft to correct for static and dynamic rotational imbalances caused by the reflector.

An alphabetical labeling is used to label sets of bodies. B identifies the set of individual bodies, W the set of reaction wheels, A the set of bodies forming the antenna assembly, and R the set of bodies with relative rotational motion about body 1:

$$B \triangleq \{1,2,3,4,5,6,7,8\}$$
$$W \triangleq \{2,3,4,5,6\}$$
$$A \triangleq \{7,8\}$$
$$R \triangleq W \cup \{A\}$$

where $\{A\}$ means that A is treated as a single body, instead of a set. For each $\lambda \in B \cup \{A\}$, a body-fixed reference frame with basis $\hat{\mathbf{e}}^\lambda$ is defined at some favorable point O^λ:

$$\mathcal{F}^\lambda \triangleq \left\{O^\lambda, \hat{\mathbf{e}}^\lambda\right\}$$

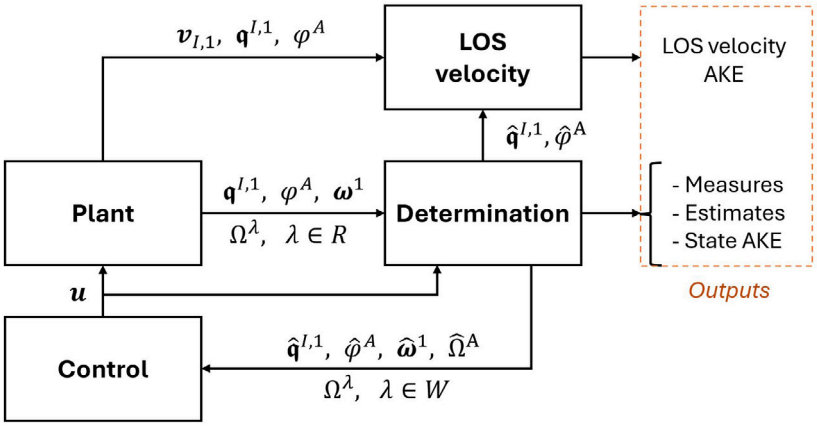

Fig. 1. Schematic of the simulation architecture, estimated quantities are indicated with a hat.

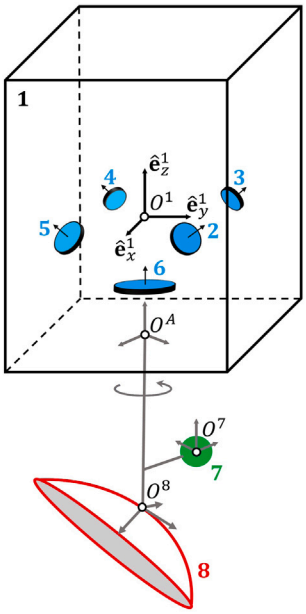

Fig. 2. Spacecraft model.

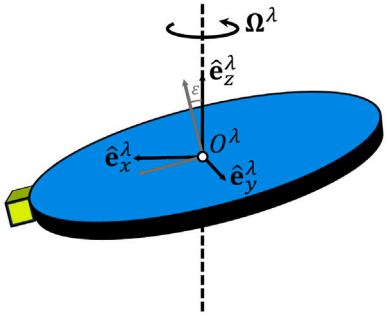

Fig. 3. Reaction wheels model.

Frame $\mathcal{F}^1$ is placed at the center of mass of body 1 and it is aligned with its principal axes of inertia. For each wheel, a frame $\mathcal{F}^\lambda$ ($\lambda \in W$) is placed at the center of mass of the wheel disk, O^λ, with axis $\hat{\mathbf{e}}_z^\lambda$ aligned with the spin direction (Fig. 3). Frame $\mathcal{F}^7$ originates at the center of mass of body 7 and may have arbitrarily oriented orthogonal axes thanks to the spherical symmetry. Frame $\mathcal{F}^8$ has the origin placed at the vertex of the parabolic reflector and axis $\hat{\mathbf{e}}_z^8$ aligned with the paraboloid axis. Frame $\mathcal{F}^A$ is fixed with the antenna assembly A at the hinge point O^A and it has axis $\hat{\mathbf{e}}_z^A$ aligned with the shaft axis.

Lastly, two additional external reference frames are defined. The first is an Earth-Centered Inertial (ECI) frame, denoted by $\mathcal{F}^I$. The second is a Local Vertical Local Horizontal (LVLH) orbital frame $\mathcal{F}^L$, with $\hat{\mathbf{e}}_z^L$ aligned with the local vertical, $\hat{\mathbf{e}}_y^L$ directed along the orbital angular momentum vector and $\hat{\mathbf{e}}_x^L$ completing the right-handed orthogonal frame.

2.2. Equations of motion

The spacecraft dynamics is modeled using the vector-dyadic representation outlined in [21, Section 3.6]. For notation, see nomenclature at the end of paper (Appendix A). Given the vector array representation of a generic basis

$$\hat{\mathbf{e}}^\lambda \triangleq \begin{bmatrix} \hat{\mathbf{e}}_x^\lambda & \hat{\mathbf{e}}_y^\lambda & \hat{\mathbf{e}}_z^\lambda \end{bmatrix}^\mathsf{T}$$

vectors are represented as $\mathbf{r} = \hat{\mathbf{e}}^{\lambda\mathsf{T}} {}^\lambda\boldsymbol{r}$, and dyadics as $\mathbf{I} = \hat{\mathbf{e}}^{\lambda\mathsf{T}} {}^\lambda\boldsymbol{I}\, \hat{\mathbf{e}}^\lambda$. Both vectors and dyadics are independent on the reference frame, thus no explicit definition of the coordinates system is needed. The coordinate system is specified only next to the column matrix of components ${}^\lambda\boldsymbol{r}$ and the matrix of components ${}^\lambda\boldsymbol{I}$, as a left superscript. Extensive explanations of the vector-dyadic formalism and operations can be found in [21, Appendix B] and [22, Chapter 2].

The dynamics model of the spacecraft includes bodies with a single rotational degree of freedom relative to body 1 (i.e., set of bodies R). Their contribution to the spacecraft dynamics also includes the effects of potential static and dynamic imbalances in rotation, introduced as forms of internal perturbations. Internal centrifugal forces and torques arise when the center of mass of body λ does not lie on the axis of rotation and when the latter is not a principal axis of inertia for body λ. Thus, the presence of these perturbations depends on the mass distribution of the rotating bodies relative to their axis of rotation. For the reaction wheels, perturbations are generated by placing a small mass at the end of the wheel disk and introducing a slight misalignment angle ϵ relative to the rotation axis (Fig. 3). In fact, this modification displaces the center of mass of the wheel from the rotation axis and results in a misalignment between this axis and one the principal axes of inertia. Following the approach in [23], the values of the small mass and the misalignment angle are determined by linking them to the static and dynamic imbalance parameters provided by reaction wheel manufacturers.

The equations of motion are derived about point O^1, which is fixed relative to body 1. The translational and absolute angular momenta of

the entire spacecraft, denoted as $\mathbf{p}$ and $\mathbf{h}_1$, are given by:

$$\mathbf{p} = m\mathbf{v}_{I,1} - m\tilde{\mathbf{r}}_{1,\bullet}\cdot\boldsymbol{\omega}^1 - \sum_{\lambda\in R} m_\lambda \tilde{\mathbf{r}}_{\lambda,\textcircled{\lambda}}\cdot\hat{\mathbf{e}}_z^\lambda \Omega^\lambda \tag{1}$$

$$\mathbf{h}_1 = m\tilde{\mathbf{r}}_{1,\bullet}\cdot\mathbf{v}_{I,1} + \mathbf{I}_1\cdot\boldsymbol{\omega}^1 + \sum_{\lambda\in R}\left(\mathbf{J}_{\lambda/1}^{(\lambda)} + \mathbf{I}_\lambda^{(\lambda)}\right)\cdot\hat{\mathbf{e}}_z^\lambda\,\Omega^\lambda \tag{2}$$

where "$\cdot$" represents an extension of the dot product to vector-dyadic operations. In the previous expression, the mass of the entire spacecraft is denoted by m, while the mass of a specific body λ is denoted by m_λ. Vector $\mathbf{r}_{1,\bullet}$ represents the displacement from point O^1 to the spacecraft center of mass $\bullet$, while vector $\mathbf{r}_{\lambda,\textcircled{\lambda}}$ represents the displacement from point O^λ to the center of mass of body λ, denoted as $\textcircled{\lambda}$. The "$\sim$" accent indicates the 3×3 skew-symmetric dyadic representation of vectors, used as replacement for cross products. The term $\mathbf{v}_{I,1}$ denotes the absolute velocity of point O^1. The absolute angular velocity of frame $\mathcal{F}^1$ is denoted by $\boldsymbol{\omega}^1$. Scalar term Ω^λ represents the magnitude of the angular velocity of frame $\mathcal{F}^\lambda$ relative to $\mathcal{F}^1$, while $\hat{\mathbf{e}}_z^\lambda$ indicates the axis of rotation. The inertia dyadic of the spacecraft about point O^1 is denoted by $\mathbf{I}_1$. This term includes the contributions of all bodies, treating the wheels and the antenna assembly as locked in their instantaneous orientation relative to frame $\mathcal{F}^1$. The inertia dyadic of body λ about O^λ is denoted by $\mathbf{I}_\lambda^{(\lambda)}$. Similarly as in [21, Section 3.6], we introduce the inertia term:

$$\mathbf{J}_{\lambda/1}^{(\lambda)} \triangleq m_\lambda\left[\left(\mathbf{r}_{\lambda,\textcircled{\lambda}}\cdot\mathbf{r}_{1,\lambda}\right)\mathbf{E} - \mathbf{r}_{\lambda,\textcircled{\lambda}}\mathbf{r}_{1,\lambda}\right] \tag{3}$$

referred to as mixed inertia dyadic of body λ, as its constituent vectors originate from two distinct points, O^λ and O^1.

Additional equations are introduced to characterize the dynamics of bodies with rotational motion relative to body 1 (i.e. $\lambda \in R$). Anticipating our needs, we first introduce the translational momentum of body λ:

$$\mathbf{p}^{(\lambda)} = m_\lambda\mathbf{v}_{I,1} - m_\lambda\tilde{\mathbf{r}}_{1,\textcircled{\lambda}}\cdot\boldsymbol{\omega}^1 - m_\lambda\tilde{\mathbf{r}}_{\lambda,\textcircled{\lambda}}\cdot\hat{\mathbf{e}}_z^\lambda\Omega^\lambda \tag{4}$$

The absolute angular momentum of any body $\lambda \in R$ is computed about hinge point O^λ to cancel out a priori the torques generated by the interbody constraint forces. Since the relative rotational motion has only one degree of freedom, the angular momentum is projected on the rotation axis $\hat{\mathbf{e}}_z^\lambda$:

$$h_{\lambda,rot}^{(\lambda)} = \hat{\mathbf{e}}_z^\lambda\cdot\left[m_\lambda\tilde{\mathbf{r}}_{\lambda,\textcircled{\lambda}}\cdot\mathbf{v}_{I,1} + \left(\mathbf{J}_{1/\lambda}^{(\lambda)} + \mathbf{I}_\lambda^{(\lambda)}\right)\cdot\boldsymbol{\omega}^1 + \mathbf{I}_\lambda^{(\lambda)}\cdot\hat{\mathbf{e}}_z^\lambda\,\Omega^\lambda\right] \tag{5}$$

where $h_{\lambda,rot}^{(\lambda)} \triangleq \hat{\mathbf{e}}_z^\lambda\cdot\mathbf{h}_\lambda^{(\lambda)}$ and $\mathbf{J}_{1/\lambda}^{(\lambda)} = \mathbf{J}_{\lambda,1}^{(\lambda)\top}$. Eqs. (1), (2) and (5) can be reformulated in the form of a matrix equation:

$$\begin{aligned}\boldsymbol{y} &= \boldsymbol{A}\boldsymbol{x}\\ \boldsymbol{x}^\top &\triangleq \left[{}^1\boldsymbol{v}_{I,1}^\top \quad {}^1\boldsymbol{\omega}^{1\top} \quad \Omega^2 \quad \cdots \quad \Omega^6 \quad \Omega^A\right]\\ \boldsymbol{y}^\top &\triangleq \left[{}^1\boldsymbol{p}^\top \quad {}^1\boldsymbol{h}_1^\top \quad h_{2,rot}^{(2)} \quad \cdots \quad h_{6,rot}^{(6)} \quad h_{A,rot}^{(A)}\right]\end{aligned} \tag{6}$$

where matrix $\boldsymbol{A}$ is shown in Box I. Note that all matrices of components in $\boldsymbol{x}$, $\boldsymbol{y}$ and $\boldsymbol{A}$ are expressed in $\mathcal{F}^1$ coordinates, as indicated by the left superscript. For clarity of notation, this superscript is omitted in $\boldsymbol{A}$. The time derivatives of the translational and angular momenta in (1), (2) and (5) expand as follows:

$$\dot{\mathbf{p}} = -\tilde{\boldsymbol{\omega}}^1\cdot\mathbf{p} + \mathbf{f} \tag{7}$$

$$\dot{\mathbf{h}}_1 = -\tilde{\boldsymbol{\omega}}^1\cdot\mathbf{h}_1 - \tilde{\mathbf{v}}_{I,1}\cdot\mathbf{p} + \boldsymbol{\tau}_1 \tag{8}$$

$$\dot{h}_{\lambda,rot}^{(\lambda)} = \hat{\mathbf{e}}_z^\lambda\cdot\left(-\tilde{\boldsymbol{\omega}}^1\cdot\mathbf{h}_\lambda^{(\lambda)} - \tilde{\mathbf{v}}_{I,\lambda}\cdot\mathbf{p}^{(\lambda)} + \boldsymbol{\tau}_\lambda^{(\lambda)}\right) \tag{9}$$

being $\mathbf{f}$ the total external force and $\boldsymbol{\tau}_1$ the total external torque about O^1, acting on the entire spacecraft. Term $\boldsymbol{\tau}_\lambda^{(\lambda)}$ represents the sum of the total torques about O^λ acting on body λ. In the present study, both gravitational and aerodynamic perturbations were considered. For translational motion, the model features only gravitational forces, neglecting the influence of aerodynamic drag on the orbit. Conversely, perturbation torques induced by both gravitational and aerodynamic forces have been implemented for the attitude. The modeling of these perturbations is presented in Appendix B.

The integration of (7), (8) and (9) yields the components of $\boldsymbol{y}$, allowing system (6) to be solved for $\boldsymbol{x}$. The attitude kinematics equations, dependent on the angular velocities in $\boldsymbol{x}$, are then integrated to determine the satellite's attitude about the inertial frame $\mathcal{F}^I$, along with the relative orientation of each body $\lambda \in R$ with respect to $\mathcal{F}^1$. The kinematics equation for the attitude are given by:

$$\begin{aligned}\dot{\mathrm{q}}^{I,1} &= \frac{1}{2}\boldsymbol{B}\left(\mathrm{q}^{I,1}\right){}^1\boldsymbol{\omega}^1\\ \dot{\mathrm{q}}^{1,\lambda} &= \frac{1}{2}\boldsymbol{B}\left(\mathrm{q}^{1,\lambda}\right){}^\lambda\boldsymbol{\Omega}^\lambda\end{aligned} \tag{10}$$

where:

$$\boldsymbol{B}(\mathrm{q}) = \begin{bmatrix} -q_1 & -q_2 & -q_3\\ q_0 & -q_3 & q_2\\ q_3 & q_0 & -q_1\\ -q_2 & q_1 & q_0\end{bmatrix}$$

being q a generic quaternion with components $\mathrm{q} = \{q_0 \;\; q_1 \;\; q_2 \;\; q_3\}^T$. Regarding translational kinematics, the motion of the spacecraft's center of mass is described by:

$$\dot{\mathbf{r}}_{I,\bullet} = \mathbf{v}_{I,\bullet} - \boldsymbol{\omega}^1\times\mathbf{r}_{I,\bullet} \tag{11}$$

which relates the absolute velocity of the center of mass, $\mathbf{v}_{I,\bullet}$, to its velocity measured relative to frame $\mathcal{F}^1$. Since the translational momentum of the spacecraft is known from the integration of the equations of motion, the absolute velocity is also known and given by $\mathbf{v}_{I,\bullet} = \mathbf{p}/m$.

2.3. Sliding mode control

A first-order sliding mode control (SMC) law is employed to maintain the spacecraft in nadir-pointing orientation and the antenna spinning at the absolute angular velocity of 12 rpm about its spin axis [7, 24]. The SMC generates the motor torques that must be applied to the reaction wheels to control the main body and to the antenna assembly for rotational control. Since the dynamics of the main body and the antenna assembly are coupled, a counterreaction torque is transferred to the main body due to the control motor torque applied to the antenna assembly. Therefore, the antenna motor torque is also included in the total control effort for the five reaction wheels.

The sliding surface $\boldsymbol{s} \in \mathbb{R}^4$ is defined as:

$$\boldsymbol{s} \triangleq \delta\boldsymbol{z} + \boldsymbol{K}_2\delta\boldsymbol{a} \tag{12}$$

where:

$$\delta\boldsymbol{z} \triangleq \begin{bmatrix}\delta\boldsymbol{\omega}^1\\ \delta\Omega^A\end{bmatrix} = \begin{bmatrix}{}^1\boldsymbol{\omega}_t^1\\ \Omega_t^A\end{bmatrix} - \begin{bmatrix}{}^1\boldsymbol{\omega}^1\\ \Omega^A\end{bmatrix} \triangleq \boldsymbol{z}_t - \boldsymbol{z} \tag{13}$$

denotes the control state error, computed as the difference between the target angular velocities $\boldsymbol{z}_t$ and the actual angular velocities $\boldsymbol{z}$. The target angular velocity ${}^1\boldsymbol{\omega}_t^1$ is set equal to the orbital angular velocity, which corresponds to the angular velocity of the LVLH frame $\mathcal{F}^L$ relative to the inertial frame $\mathcal{F}^I$. Ω_t^A represents the target angular velocity of the antenna and it is set equal to 12 rpm. The attitude error, $\delta\boldsymbol{a}$, is expressed as:

$$\delta\boldsymbol{a} = \begin{bmatrix}\delta\boldsymbol{q}^{I,1}\\ \delta\varphi^A\end{bmatrix} \tag{14}$$

The first three components, represented by $\delta\boldsymbol{q}^{I,1}$, denote the vectorial part the of quaternion error

$$\delta\mathrm{q}^{I,1} = \begin{bmatrix}\delta q_0^{I,1}\\ \delta\boldsymbol{q}^{I,1}\end{bmatrix} = \mathrm{q}_t^{I,1*}\otimes\mathrm{q}^{I,1}$$

which describes the attitude error between the target body frame and the actual body frame $\mathcal{F}^1$. This error is computed as the quaternion

$$\boldsymbol{A} \triangleq \begin{bmatrix} m\boldsymbol{E} & -m\tilde{\boldsymbol{r}}_{1,\textcircled{\scriptsize 1}} & -m_2\,\tilde{\boldsymbol{r}}_{2,\textcircled{\scriptsize 2}}\,\hat{\boldsymbol{e}}_z^2 & \cdots & -m_6\,\tilde{\boldsymbol{r}}_{6,\textcircled{\scriptsize 6}}\,\hat{\boldsymbol{e}}_z^6 & -m_A\,\tilde{\boldsymbol{r}}_{A,\textcircled{\scriptsize A}}\,\hat{\boldsymbol{e}}_z^A \\ m\tilde{\boldsymbol{r}}_{1,\textcircled{\scriptsize 1}} & \boldsymbol{I}_1 & \left(\boldsymbol{J}_{2/1}^{(2)}+\boldsymbol{I}_2^{(2)}\right)\hat{\boldsymbol{e}}_z^2 & \cdots & \left(\boldsymbol{J}_{6/1}^{(6)}+\boldsymbol{I}_6^{(6)}\right)\hat{\boldsymbol{e}}_z^6 & \left(\boldsymbol{J}_{A/1}^{(A)}+\boldsymbol{I}_A^{(A)}\right)\hat{\boldsymbol{e}}_z^A \\ m_2\,\hat{\boldsymbol{e}}_z^{2\top}\tilde{\boldsymbol{r}}_{2,\textcircled{\scriptsize 2}} & \hat{\boldsymbol{e}}_z^{2\top}\left(\boldsymbol{J}_{1/2}^{(2)}+\boldsymbol{I}_2^{(2)}\right) & \hat{\boldsymbol{e}}_z^{2\top}\boldsymbol{I}_2^{(2)}\hat{\boldsymbol{e}}_z^2 & \cdots & 0 & 0 \\ \vdots & \vdots & \vdots & \ddots & \vdots & 0 \\ m_6\,\hat{\boldsymbol{e}}_z^{6\top}\tilde{\boldsymbol{r}}_{6,\textcircled{\scriptsize 6}} & \hat{\boldsymbol{e}}_z^{6\top}\left(\boldsymbol{J}_{1/6}^{(6)}+\boldsymbol{I}_6^{(6)}\right) & 0 & \cdots & \hat{\boldsymbol{e}}_z^{6\top}\boldsymbol{I}_6^{(6)}\hat{\boldsymbol{e}}_z^6 & 0 \\ m_A\,\hat{\boldsymbol{e}}_z^{A\top}\tilde{\boldsymbol{r}}_{A,\textcircled{\scriptsize A}} & \hat{\boldsymbol{e}}_z^{A\top}\left(\boldsymbol{J}_{1/A}^{(A)}+\boldsymbol{I}_A^{(A)}\right) & 0 & 0 & 0 & \hat{\boldsymbol{e}}_z^{A\top}\boldsymbol{I}_A^{(A)}\hat{\boldsymbol{e}}_z^A \end{bmatrix}$$

Box I.

product between the conjugate of the target quaternion and the quaternion aligning $\mathcal{F}^I$ to frame $\mathcal{F}^1$. The target quaternion is defined as the one that aligns frame $\mathcal{F}^I$ to the LVLH frame $\mathcal{F}^L$. The fourth component in (14), $\delta\varphi^A$, denotes the antenna azimuthal error. The gain matrix $\boldsymbol{K}_2 \in \mathbb{R}^{4\times4}$ is a diagonal matrix whose coefficients must be tuned to achieve the desired system behavior.

To formulate the control law, the time derivative of $\boldsymbol{s}$ is set equal to a sigmoid function of $\boldsymbol{s}$ designed to make the sliding function attractive for the system trajectory:

$$\dot{\boldsymbol{s}} = \delta\dot{\boldsymbol{z}} + \boldsymbol{K}_2\delta\dot{\boldsymbol{a}} = -\boldsymbol{K}_1\tanh(\eta\boldsymbol{s}) \tag{15}$$

where $\boldsymbol{K}_1 \in \mathbb{R}^{4\times4}$ is a second tunable diagonal gain matrix and η an additional tuning parameter, used for chattering mitigation. By employing the relation for $\delta\dot{\boldsymbol{q}}^{I,1}$ from [25], the time derivative of the attitude error can be expressed as:

$$\delta\dot{\boldsymbol{a}} = \begin{bmatrix} \frac{1}{2}\left\{\delta q_0^{I,1}\delta\boldsymbol{\omega}^1 + \delta\boldsymbol{q}^{I,1}\times\left(\delta\boldsymbol{\omega}^1+2\boldsymbol{\omega}^1\right)\right\} \\ \delta\Omega^A \end{bmatrix} \tag{16}$$

The time derivative of the control state error $\delta\dot{\boldsymbol{z}}$ requires expressions for both the target state derivative, $\dot{\boldsymbol{z}}_t$, and the control state derivative, $\dot{\boldsymbol{z}}$. The latter involves an explicit derivation of the spacecraft attitude dynamics, where $\dot{\boldsymbol{z}}$ is expressed as a function of the control state $\boldsymbol{z}$ and the control input $\boldsymbol{u}$. This is achieved by substituting the expressions of translational and angular momenta in the equations of dynamics (7), (8) and (9), while adopting a simplified model of the spacecraft dynamics. In particular, the simplified model presents a perfectly balanced antenna and wheels, without perturbation torques acting on the spacecraft. Due to the length of the mathematical steps, the complete derivation will be provided in Appendix C. By expanding these equations and rewriting everything in matrix form (as in [19]), we obtain:

$$\boldsymbol{M}\dot{\boldsymbol{z}} = \boldsymbol{g} - \boldsymbol{u} \tag{17}$$

where $\boldsymbol{M}$, $\boldsymbol{g}$ and $\boldsymbol{u}$ are defined in Appendix C. Substituting the previous relationship into (15) and solving explicitly for $\boldsymbol{u}$, yields the control law:

$$\boldsymbol{u} = \boldsymbol{g} - \boldsymbol{M}\left[\dot{\boldsymbol{z}}_t + \boldsymbol{K}_2\delta\dot{\boldsymbol{a}} + \boldsymbol{K}_1\tanh(\eta\boldsymbol{s})\right] \tag{18}$$

According to definition (C.14), the first three components of the control torque $\boldsymbol{u}$ represent the motor torques that must be distributed across the five reaction wheels, while the fourth component $u_4 = -u^{(A)}$ represents the opposite of the motor torque applied to the antenna assembly. Considering that, by choice, wheel 6 is devoted to counteracting motor torques acting on the antenna assembly, the motor torque exerted on it will be:

$$u^{(6)} = u_4$$

while the motor torques acting on the other four reaction wheels will be:

$$\begin{Bmatrix} u^{(2)} & u^{(3)} & u^{(4)} & u^{(5)} \end{Bmatrix}^T = \boldsymbol{T}^{p,1}\left(\boldsymbol{u}_{1:3} - u_4\,{}^1\hat{\boldsymbol{e}}_z^6\right)$$

being $\boldsymbol{T}^{p,1}$ the $\mathbb{R}^{4\times3}$ matrix converting from $\mathcal{F}^1$ coordinates to pyramidal configuration (see Fig. 2) coordinates.

3. Attitude determination architecture

Fig. 4 shows the details of the determination block from Fig. 1. In the following paragraphs, the different components of this system are discussed.

A full suite of sensors, chosen accordingly to the WIVERN Report for Assessment [7], provide the measurements for the main body attitude and angular velocity estimation, and of the single-axis rotation of the antenna assembly:

1. A triaxial gyroscope, or gyro, measures the angular velocity of body 1 with respect to the inertial frame. In particular, a Fiber Optic Gyroscope (FOG) was chosen.
2. An absolute rotary encoder measures the absolute angular position of the antenna assembly rotor with respect to a stator attached to the main body 1 in correspondence of hinge point O^A.
3. A medium range star tracker (ST) with three optical heads, which measures the spacecraft attitude with respect to the inertial reference frame by observing a sector of the sky with a camera and identifying fixed stars. Each one of the three star cameras (SCs), directly measure the rotation quaternion from the inertial frame to their respective frames, defined based on how they are mounted with respect to the main body. Then multiple measurements are merged together to provide the state observer with a single measured attitude quaternion $\mathrm{q}^{I,1}$. In missions like WIVERN with high performance requirements for attitude determination and control, star trackers are mandatory.

Measurements from these sensors are inputs of an Extended Kalman Filter (EKF), adopted as the state observer algorithm for this project. Kalman filters are recursive algorithms used to solve the state estimation problem, i.e. finding the best estimate of a system by using a set of measurements and a model of the system dynamics, which are both affected by random errors. Kalman filters are commonly associated with attitude determination and control systems. In the Extended Kalman Filter, the system dynamics are linearized at each step for the computation of the state estimate [26]. These algorithms are discrete and recursive, as computations at the discrete time t_k depend on information on the previous iteration at t_{k-1}.

3.1. Sensor models

3.1.1. Gyroscope

The 3-axis gyroscope is modeled as an inertial sensor with systematic and quantization error [27] plus a bias and a noise term [28,29]. The measured angular velocity in frame $\mathcal{F}^1$, for a given true angular velocity ${}^1\boldsymbol{\omega}^1$, can be expressed as

$${}^1\boldsymbol{\omega}^1_{meas} = {}^1\boldsymbol{\omega}^1 + \boldsymbol{G}_{\boldsymbol{\omega}}\boldsymbol{T}_{\boldsymbol{\omega}}\,{}^1\boldsymbol{\omega}^1 + \boldsymbol{w}_{\boldsymbol{\omega}} + \boldsymbol{b}_{\boldsymbol{\omega}} + \boldsymbol{n}_{\boldsymbol{\omega}} \tag{19}$$

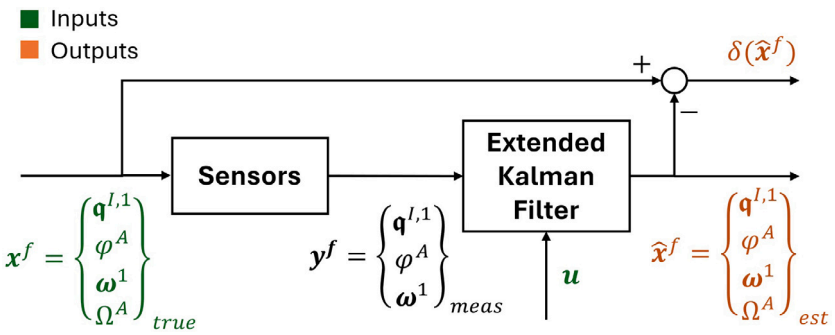

Fig. 4. Schematic of the attitude determination architecture.

Table 1
Gyro specifications taken from [31].

Parameter	Symbol	Value
Sample rate	f_ω	200 [Hz]
Full scale	$\pm\omega_{max}$	±15 [deg/s]
Misalignment	$\Delta\theta_\omega$	25 [μrad]
Scale error max	Δ_ω	40 [ppm]
ARW	W_ω	10^{-4} [deg/$\sqrt{\text{h}}$]
Bias stability over 1 h	β_ω	2×10^{-4} [deg/h]
Resolution	N^ω_{bits}	32 bits

Table 2
Rotary encoder specifications [37].

Parameter	Symbol	Value
Sample rate	f_{enc}	8 [KHz]
Radius	r_{enc}	10.16 [cm]
Resolution	N^{enc}_{bits}	25 [bits]
White noise covariance	σ_{enc}	0.64 [arcsec^2]

The real angular velocity term ${}^1\boldsymbol{\omega}^1$, obtained through the equations of motion, is scaled by the scale error matrix $\boldsymbol{G}_\omega = \Delta_\omega\, \boldsymbol{E}_3$, with $\boldsymbol{E}_3$ being the identity matrix, and rotated around the 3 axes by the small angle $\Delta\theta_\omega$, representing a misalignment error, with the matrix $\boldsymbol{T}_{\boldsymbol{\omega}}$. The term $\boldsymbol{w}_{\boldsymbol{\omega}}$ is a white Gaussian noise with covariance $\sigma^2_\omega = W^2_\omega f_\omega$, where f_ω is the sensor sample rate and W_ω is the Angular Random Walk (ARW) of the gyroscope. The term $\boldsymbol{b}_{\boldsymbol{\omega}}$ represents the systematic errors of the gyroscope, which is modeled with two components, one static and one time changing:

$$\boldsymbol{b}_{\boldsymbol{\omega}} = \boldsymbol{b}_0 + \int_{t_0}^{t_1} \boldsymbol{\eta}_\beta dt, \tag{20}$$

where the first term $\boldsymbol{b}_0$ is the constant initial bias, which usually is calibrated out, and the second term represents a bias drift, often modeled as a first order random walk [30] with $\boldsymbol{\eta}_\beta$ being a white Gaussian noise with covariance $\sigma^2_\eta = \beta^2_\omega f_\omega / \Delta t_\beta$.

The term $\boldsymbol{n}_\omega$ represents the quantization noise, due to the discretization of the continuous signal acquired by the sensor with a given number of bits, N^ω_{bits} [27]. In Table 1 the adopted gyro specifications are presented.

3.1.2. Rotary encoder

The absolute rotary encoder measures the rotation angle around the axis $\hat{\mathbf{e}}^A_z$ by which the antenna assembly A has moved [32–35]. Sensor errors in the measurement model mainly consist of noise in our case, as adoption of two sensing heads allows for elimination of all major sinusoidal systematic error terms due to eccentricity [36]. The measured absolute angular position, given a true absolute angle of rotation φ^A_{true}, is expressed by:

$$\varphi^A_{meas} = \varphi^A_{true} + w_\varphi + n_\varphi \tag{21}$$

The two terms represent, respectively, the Gaussian white noise term with covariance σ^2_{enc} (w_φ) and the quantization error term (n_φ). The adopted encoder specifications are presented in Table 2.

3.1.3. Star tracker

The Star Tracker measurement model is based on research about ST cameras noise characteristics and fusion of multiple optical heads in [27,38–41], in combination with terminology and performance specifications provided by the ECSS document [42]. The star tracker consists of three star cameras (or optical heads), which in the following paragraphs are referred to using the numbers $\mathbb{1}, \mathbb{2}$ and $\mathbb{3}$ (in order to avoid confusions with bodies 1, 2 and 3). Following the steps outlined in [41], $\mathfrak{q}^{I,1}_{\alpha,meas}$, i.e. the attitude quaternion representing the rotation from the inertial frame to the body frame $\mathcal{F}^1$ measured from a singular star camera $\alpha = \mathbb{1}, \mathbb{2}, \mathbb{3}$, can be expressed with the quaternion product:

$$\mathfrak{q}^{I,1}_{\alpha,meas} = \mathfrak{q}^{I,1}_{\alpha,true} \otimes \mathfrak{q}^{I,1}_{\alpha,err} \tag{22}$$

As the measurement error quaternion corresponds to small angle rotations, it can be expressed normalizing the quaternion

$$\mathfrak{q}^{I,1}_{\alpha,err} \approx \left\{1,\ \frac{1}{2}\,{}^\alpha\boldsymbol{\epsilon}_\alpha\right\}^T$$

where the vector of small angles $\boldsymbol{\epsilon}_\alpha$ is expressed in the camera α frame $\mathcal{F}^\alpha$, and in body frame $\mathcal{F}^1$ as ${}^1\boldsymbol{\epsilon}_\alpha = \boldsymbol{T}^{1,\alpha}\,{}^\alpha\boldsymbol{\epsilon}_\alpha$. Independently from the considered camera, the three small components of $\boldsymbol{\epsilon}$ can defined as follows [39,40,42]:

$$\boldsymbol{\epsilon} = \boldsymbol{\epsilon}_{bias} + \boldsymbol{\epsilon}_{TE}(T) + \boldsymbol{\epsilon}_{FSE} + \boldsymbol{\epsilon}_{PSE} + \boldsymbol{\epsilon}_{TN} \tag{23}$$

where:

- $\boldsymbol{\epsilon}_{bias}$ is the bias term which can be due to catalogue errors, on-ground calibration residuals, launch-induced misalignment and degradation with age.
- $\boldsymbol{\epsilon}_{TE}(T) = \boldsymbol{\epsilon}_{TE,t}\Delta T$ represents the thermo-elastic errors due to deformations associated to temperature variations. It is assumed that this term changes linearly with $\Delta T = T - T_0$ where T_0 is the mean value of the operating temperature range. In absence of thermal modeling, a worst case can be adopted using a constant value of ΔT_{max} corresponding to the limits of the operating range, adopting $\boldsymbol{\epsilon}_{TE}(T) = \boldsymbol{\epsilon}^{max}_{TE} = \boldsymbol{\epsilon}_{TE,T}\Delta T_{max}$ independently of temperature. The maximum systematic error of the star tracker therefore is given by $\boldsymbol{\epsilon}^{max}_{sys} = \boldsymbol{\epsilon}_{bias} + \boldsymbol{\epsilon}^{max}_{TE}$.
- $\boldsymbol{\epsilon}_{FSE}$ and $\boldsymbol{\epsilon}_{PSE}$ terms represent, respectively, the field of view (FOV) spatial error (FSE) and pixel spatial error (PSE). As outlined in [43], these two spatial error terms $\boldsymbol{\epsilon}_s$ can be both modeled as a first order Gauss–Markov process [44]:

  $$\dot{\boldsymbol{\epsilon}}_s = \tau_s^{-1}\boldsymbol{\epsilon}_s + \mathbf{w}_s \qquad s = \text{FSE or PSE}$$

  where τ_s is the process correlation time and $\mathbf{w}_s$ is a zero-mean Gaussian white noise with covariance $2\sigma^2_s\tau_s^{-1}$. The correlation times τ_{FSE} and τ_{PSE} are defined as the time needed for a star to cross, respectively, the star camera field of view and one pixel on the detector.

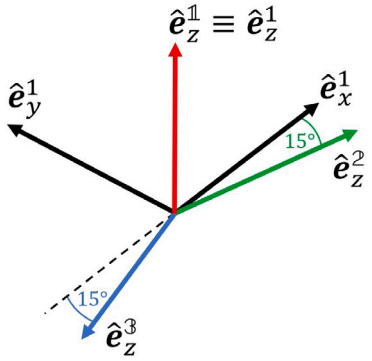

Fig. 5. Representation of the SCs boresights configuration with respect to frame $\mathcal{F}^1$ with the body frame axes in black and the SCs boresight axes in red, green and blue ($\hat{e}_z^{\mathbb{2}}$ and $\hat{e}_z^{\mathbb{3}}$ are orthogonal to $\hat{e}_z^{\mathbb{1}}$). (For interpretation of the references to color in this figure legend, the reader is referred to the web version of this article.)

- ϵ_{TN} represents the temporal noise, which is modeled as a zero-mean Gaussian white noise with covariance σ_{TN}^2.

Errors are expressed as three angles around the star camera frame axes, where the z-axis corresponds to the camera boresight: σ_{FSE}, σ_{PSE} and σ_{TN} terms are around one order of magnitude greater around the boresight axis.

Three separate cameras are considered, so $\alpha = \mathbb{1}, \mathbb{2}, \mathbb{3}$. Assuming that all errors are Gaussian in nature, the optimal fusion between the three measured quaternions, can be obtained by using a least-squares adjustment that takes into account the higher inaccuracies around the boresight axis [41]:

$$\mathrm{q}_{opt}^{I,1} = \mathrm{q}_{\mathbb{1},meas}^{I,1} \otimes \left\{ 1,\ \frac{1}{2} \boldsymbol{P}_{tot}^{-1} \sum_{\alpha=\mathbb{2}}^{\mathbb{3}} \boldsymbol{P}_\alpha \Delta\boldsymbol{\epsilon}_{\mathbb{1}\alpha} \right\}^T \tag{24}$$

where:

- $\Delta\boldsymbol{\epsilon}_{\mathbb{1}\alpha} = {}^1\boldsymbol{\epsilon}_\alpha - {}^1\boldsymbol{\epsilon}_{\mathbb{1}}$ is the angular offset between measurement quaternion pairs, as they are close to each other: $\mathrm{q}_{\mathbb{1}}^{-I,1} \otimes \mathrm{q}_\alpha^{I,1} = \left\{ 1,\ \frac{1}{2}\Delta\boldsymbol{\epsilon}_{\mathbb{1}\alpha} \right\}^T$
- $\boldsymbol{P}_\alpha$ is a weighing matrix defined as:

$$\boldsymbol{P}_\alpha = \boldsymbol{T}^{1,\alpha} \begin{bmatrix} \frac{1}{\sigma_{\alpha,x}^2} & 0 & 0 \\ 0 & \frac{1}{\sigma_{\alpha,y}^2} & 0 \\ 0 & 0 & \frac{1}{\sigma_{\alpha,z}^2} \end{bmatrix} \boldsymbol{T}^{\alpha,1}$$

where $\sigma_{\alpha,i}^2$ are the noise covariances around each axis $i = x, y, z$ of the star camera $\mathcal{F}^\alpha$ frame. Consequently, $\boldsymbol{P}_{tot} = \sum_{\alpha=1}^{3} \boldsymbol{P}_\alpha$.

As spatial noise components have higher PSD at lower frequencies and are therefore not strictly Gaussian, some trial and error tuning is required for matrix $\boldsymbol{P}_\alpha$. The terms $\sigma_{\alpha,i}^2$, regardless of α, have been set equal to the following values:

$$\sigma_{\alpha,x}^2 = 1.4 \times 10^9, \quad \sigma_{\alpha,y}^2 = 2.2 \times 10^{10}, \quad \sigma_{\alpha,z}^2 = 5.7 \times 10^4$$

In Table 3 the ST specifications are presented: values indicated are end-of-life worst cases, adopted as the conservative option.

The three star cameras $\mathcal{F}^\alpha$ frames are obtained rotating the main body frame $\mathcal{F}^1$:

- Star camera 1 frame $\mathcal{F}^{\mathbb{1}}$ corresponds to frame $\mathcal{F}^1$;
- Star camera 2 frame $\mathcal{F}^{\mathbb{2}}$ is obtained with a rotation of $\theta_{\mathbb{2}} = 90$ deg around y and $\varphi_{\mathbb{2}} = 15$ deg around x;F
- Star camera 3 frame $\mathcal{F}^{\mathbb{3}}$ is obtained with a rotation of $\theta_{\mathbb{3}} = -90$ deg around y and $\varphi_{\mathbb{3}} = 15$ deg around x (see Fig. 5).

The three cameras are positioned on the edge between the +z and −y faces of the main body, so the body of the spacecraft is always excluded from the view of the sensors. While star camera $\mathbb{1}$ is always directed towards the zenith direction, Earth is assumed to always be out of view of star cameras $\mathbb{2}$ and $\mathbb{3}$. This assumption is justified considering the disposition of the two cameras, their FOVs, their Earth Exclusion Angle (EEA), the satellite geometry and its altitude h of 500 km. The cameras half FOV is smaller than the angle from the closest spacecraft face $\varphi_{\mathbb{2}}$ and $\varphi_{\mathbb{3}}$, while the EEA angle of 18.5 deg is less than the angular distance of the two boresights from the horizon approximately equal to 90 - $\beta_E/2 \approx 22$ deg, where $\beta_E = 2sin^{-1}\left(\frac{R_E}{R_E+h}\right) \approx 136$ deg is Earth's angular diameter as seen from orbit (assuming a spherical Earth). Furthermore, as the spacecraft is in a dusk-to-dawn sun-synchronous orbit [7] and the attitude is kept aligned with the local orbital frame $\mathcal{F}^L$, placing the boresights on the edge between the +z and −y face and away from them allows for the assumption that the Sun is always outside of the sensors field of view. After trial and error experimentation using different orientations, this configuration was also found to improve performances, i.e. the results that will be presented in Section 4.

Table 3
Star tracker specifications for single camera with boresight on the z-axis [45,46].

Parameter	Value
f_{ST}	20 [Hz]
SCs α	1, 2, 3
FOV	23 [deg]
N_{pixel} (across)	1024
T_{min}, T_{max} (operational)	−30, +60 [°C]
ϵ_{bias} (all axes)	11 [arcsec]
$\epsilon_{TE,T}$ (all axes)	0.055 [arcsec/K]
σ_{FSE} across the z-axis	0.2 [arcsec]
σ_{FSE} around the z-axis	1.53 [arcsec]
σ_{PSE} across the z-axis	1.33 [arcsec]
σ_{PSE} around the z-axis	9 [arcsec]
σ_{TN} across the z-axis	0.77 [arcsec]
σ_{TN} around the z-axis	6 [arcsec]
EEA	18.5 [deg]

3.2. Extended Kalman filter

To present the EKF algorithm and the problems to be addressed for its implementation, a general discrete state-space formulation of a dynamical system at time t_k is adopted, as discussed in [26]:

$$\begin{aligned} \dot{\boldsymbol{x}}_k &= f\left(\boldsymbol{x}_k, \boldsymbol{u}_k\right) + \boldsymbol{d}_k^x \\ \boldsymbol{y}_k &= h\left(\boldsymbol{x}_k\right) + \boldsymbol{d}_k^y \end{aligned} \tag{25}$$

The goal of a filter algorithm is to obtain at the discrete time t_k an accurate estimate $\hat{\boldsymbol{x}}_k$ of the true state $\boldsymbol{x}_k$, which is not directly known, based on past values of $\hat{\boldsymbol{x}}_k$, and on the output and input vectors, respectively $\boldsymbol{y}_k$ and $\boldsymbol{u}_k$, which are all known quantities. Terms $\boldsymbol{d}_k^x$ and $\boldsymbol{d}_k^y$ represent disturbances to the state and output, both assumed to be zero mean Gaussian white noise. Functions h and f map, respectively, the state and input vectors to the output and the derivative of the state. After choosing an initial state estimate $\hat{\boldsymbol{x}}_0$ and initial estimation error covariance matrix $\boldsymbol{P}_0$, the EKF algorithm is structured in two steps [26]:

1. **Prediction**
   The state estimate and covariance matrix are propagated based on information from the previous iteration (a forward Euler integration scheme is adopted, where τ_f is the filter sample time). The matrix $\boldsymbol{Q}$ represents the process noise covariance matrix.

$$\begin{aligned} \boldsymbol{x}_k^p &= \hat{\boldsymbol{x}}_{k-1} + \tau_f\ f\left(\hat{\boldsymbol{x}}_{k-1}, \boldsymbol{u}_{k-1}\right) \\ \boldsymbol{P}_k^p &= \boldsymbol{F}_{k-1} \boldsymbol{P}_{k-1} \boldsymbol{F}_{k-1}^T + \boldsymbol{Q} \end{aligned}$$

2. **Update**
   State estimate and covariance matrix are updated based on the prediction and on current information from the measurements. In this step,

Table 4
EKF filter parameters and initialization values (Q and R are diagonal matrices with main diagonal elements in parenthesis).

Parameter	Value
f_{ekf}	10 [Hz]
$\boldsymbol{Q}$	$10^{-11} \times diag(1,1,1,1,1,100,100,100,1)$
$\boldsymbol{R}$	$10^{-9} \times diag(10,10,10,10,0.1,0.1,0.1,1)$
$\boldsymbol{H}$	$[\boldsymbol{E}_8, \ \boldsymbol{0}_{8,1}]$
$\boldsymbol{x}_0^f$	$[1, \ \boldsymbol{0}_{7,1}, \ \Omega_0^6]^T$
$\boldsymbol{P}_0$	$\boldsymbol{E}_9$

the Kalman gain $\boldsymbol{K}$ is computed, chosen to minimize the estimation error norm $\|\boldsymbol{x}_k - \hat{\boldsymbol{x}}_k\|^2$:

$$\boldsymbol{K}_k = \boldsymbol{P}_k^p \boldsymbol{H}_k^T \left(\boldsymbol{H}_k \boldsymbol{P}_k^p \boldsymbol{H}_k^T + \boldsymbol{R}\right)_k^{-1}$$
$$\Delta \boldsymbol{y}_k = \boldsymbol{y}_k - h\left(\boldsymbol{x}_k^p\right)$$
$$\hat{\boldsymbol{x}}_k = \boldsymbol{x}_k^p + \boldsymbol{K}_k \Delta \boldsymbol{y}_k$$
$$\boldsymbol{P}_k = \left(\boldsymbol{E}_n - \boldsymbol{K}_k \boldsymbol{H}_k\right) \boldsymbol{P}_k^p$$

$\boldsymbol{R}$ is the measurement noise covariance matrix. For this study, the state and measurement vectors, respectively $\boldsymbol{x}^f$ (with apex "f" to differentiate from Eq. (6)) and $\boldsymbol{y}^f$, entering the filter algorithm are defined as:

$$\boldsymbol{x}^f = \left\{\mathrm{q}^{I,1} \quad \varphi^A \quad \boldsymbol{\omega}^1 \quad \Omega^A\right\}^T$$
$$\boldsymbol{y}^f = \left\{\mathrm{q}_{meas}^{I,1} \quad \varphi_{meas}^A \quad \boldsymbol{\omega}_{meas}^1\right\}^T$$

The function h is simply defined as $h(\boldsymbol{x}^f) = \left\{\mathrm{q}_{I1} \quad \varphi^A \quad \boldsymbol{\omega}^1\right\}^T$, so the measurement matrix $\boldsymbol{H}$, obtained as the Jacobian of h computed in $\hat{\boldsymbol{x}}_k$, is a constant 8×9 matrix. As it can be noted, Ω^A is part of the estimation process as it is necessary for the state propagation step, but it is not a measured quantity, therefore its value is obtained directly from the EKF algorithm. The definition of the function f has to be addressed, from which the state propagation matrix $\boldsymbol{F}_k$ can be computed:

$$\boldsymbol{F}_k \triangleq 1 + \tau_f \left.\frac{\partial f(\boldsymbol{x})}{\partial \boldsymbol{x}}\right|_{\boldsymbol{x}=\hat{\boldsymbol{x}}_k}$$

where $\frac{\partial f(\boldsymbol{x})}{\partial \boldsymbol{x}}$ is the Jacobian of f computed in $\hat{\boldsymbol{x}}_k$.

For the time evolution of the angular velocities, the simplified model approach considered in Section 2.3 and shown in dept in Appendix C is adopted, which is similar to the approach that can be found in [18,19] for the filter algorithm. The complete form of f considers the antenna assembly rotation and the attitude quaternion kinematics (see Eq. (10)) in the time evolution of the filter states:

$$\dot{\boldsymbol{x}}^f = \begin{Bmatrix} \dot{\mathrm{q}}^{I,1} \\ \dot{\varphi}^A \\ \dot{\boldsymbol{\omega}}^1 \\ \dot{\Omega}^A \end{Bmatrix} = \begin{Bmatrix} \dot{\mathrm{q}}^{I,1} \\ \dot{\varphi}^A \\ \dot{\boldsymbol{z}} \end{Bmatrix} = \begin{Bmatrix} \frac{1}{2}\boldsymbol{B}(\mathrm{q}^{I,1})\,\boldsymbol{\omega}^1 \\ \Omega^A \\ \boldsymbol{M}^{-1}\,(\boldsymbol{g} - \boldsymbol{u}) \end{Bmatrix} = f\left(\boldsymbol{x}^f, \ \boldsymbol{u}, \ \boldsymbol{\Gamma}\right)$$

where $\boldsymbol{\Gamma} = \left\{\Omega^2, \ ..., \ \Omega^5\right\}^T$ is a vector containing the known reaction wheels angular velocities.

Filter parameters are specified in Table 4. The sample rate of the filter has been fixed in order to have all sample rates of the sensors be an integer multiple of the filter frequency. At the time instant the filter computes an estimate, only the latest measurement from the sensor is taken into account.

4. Simulation and results

The numerical simulator has been developed in the MATLAB/Simulink computational environment. For integration of the equations of motion the 5th order Dormand-Prince method was used, while Forward Euler integration was used for components in discrete time. A large gamut of simulation studies have been performed, which are briefly presented in this paragraph.

1. *Nominal simulation*: aimed at assessing the outputs of simulation with a set of given system parameters (see tables Appendix D), within a total time span of two orbits. The antenna is considered balanced, reaction wheels are unbalanced (resulting in jitter effects), and sensor include both systematic and random errors. Results shown are the Absolute Knowledge Error (AKE) of the three measured states $\mathrm{q}^{I,1}$, ${}^1\boldsymbol{\omega}^1$, φ^A, and the line-of-sight velocity ${}_{los}v_{I,1}$, defined as the projection of $\mathbf{v}_{I,1}$ along the antenna boresight axis $\hat{\mathbf{e}}_z^8$.
2. *Antenna unbalances*: study of the effect of unbalances in the antenna assembly, specifically by varying mass and position of body 7. Other system properties are kept the same as in the nominal simulations.
3. *Star tracker systematic error*: study of the effect of variations of the component $\boldsymbol{\varepsilon}_{sys} = \boldsymbol{\varepsilon}_{bias} + \boldsymbol{\varepsilon}_{TE}$ from Eq. (23). A total of nine parameters are considered, one for each axis of the three star cameras. Other system properties are kept the same as in the nominal simulations.

For both antenna unbalance and ST systematic error analyses, two sets of simulations have been performed. First, a campaign to assess the worst cases, adopting all possible combinations of the set of free parameters is considered. Then, a Monte Carlo campaigns was carried out to assess the sensitivity and robustness of the system to random errors.

Nominal simulation parameters and initial conditions can be found in the tables in Appendix D.

4.1. Nominal

The results of the filter performance in normal operating conditions are presented. Parameters are included in Appendix D: the antenna is considered balanced, reaction wheels are unbalanced (resulting in jitter effects), while both systematic and random errors are considered for the sensors. EKF outputs regarding the states are shown in Fig. 6: attitude (expressed in terms of the Euler angles), angular velocity ${}^1\boldsymbol{\omega}^1$, and antenna angle φ^A. To include two orbits, a total simulation time of 11 400 s (≈2 h) was adopted, as the orbital period is roughly equal to 5677 s. In the nominal case, the systematic error of the ST has been fixed to a positive value of $\boldsymbol{\varepsilon}_{sys}$ for all axes of the star cameras frames, except for axis $\hat{\mathbf{e}}_x^2$, where it has been put to $-\boldsymbol{\varepsilon}_{sys}$. This choice followed from trial and error, as it showed the highest absolute values of LOS velocity AKE (see also following discussion in Section 4.3 for a more in depth analysis on the ST systematic errors).

Once settled, the Euler angles AKE remain roughly constant, with minimal random variations and absolute value confined under 70 μrad, while the envelope of the antenna angle AKE $\delta(\varphi^A)$ is bounded between ±10 μrad. The angular velocity AKE remains lower than 3 μrad/s, which is approximately 0.27% of the constant angular velocity for the spacecraft in nadir-pointing attitude, approximately equal to 0.0011 rad/s.

Fig. 7 presents results for the AKE of the line-of-sight velocity, which is the key quantity analyzed in this study. To compute such variable, true and estimated values of $\mathrm{q}^{I,1}$ and φ^A are used to transform the antenna boresight axis $\hat{\mathbf{e}}_z^8$ and the orbital velocity vector $\boldsymbol{v}_{I,1}$ in the same frame. Then, the velocity component along the true and estimated boresight axis are subtracted to obtain the AKE signal. Line-of-sight velocity plots are capped by the requirement value of ±1 m/s on the y-axis. A 15 s zoomed detail of the plot is displayed in the inset in order to show the behavior of the signal on short time scales. As the AKE values strongly depends on the angular position of the antenna, the short term structure is mainly dominated by sinusoidal signals with frequencies that are multiples of the rotation period.

In Fig. 8 the impact of filtering can be better appreciated in the frequency domain. At higher frequencies the PSD of $\delta({}_{los}v_{I,1})$ obtained after the filtering process is lower than the one obtained with velocity values calculated using directly the sensors outputs, i.e. the unfiltered measurements. Starting around 10^{-1} Hz, the ratio between the PSDs of the two signals falls off roughly −9 dB per decade. Additionally,

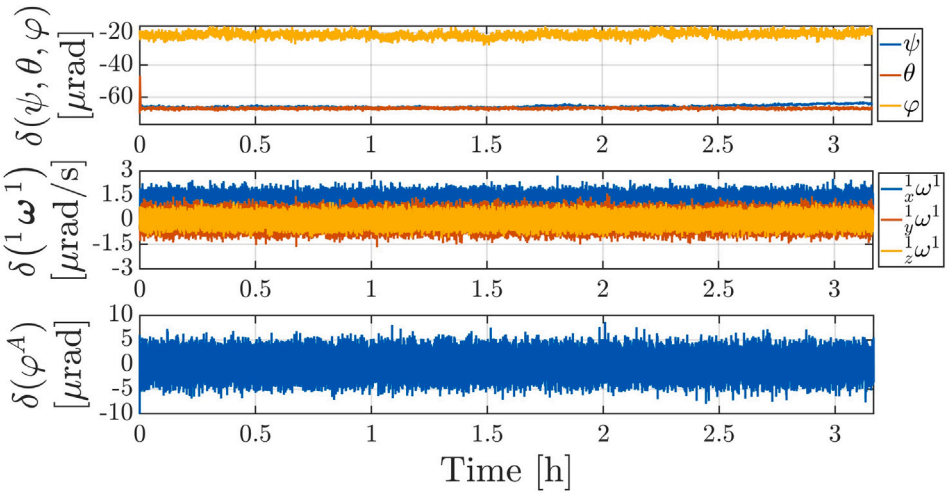

Fig. 6. Time evolution of the states Absolute Knowledge Error (indicated by the symbol δ) for a total simulation time of two orbital periods.

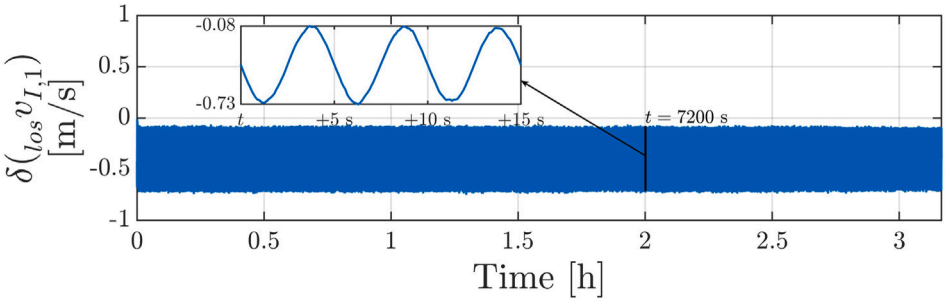

Fig. 7. Time evolution of the line-of-sight velocity AKE for a total simulation time of two orbital periods. The zoomed inset shows the short term structure of the signal: a sinusoid with mean value $\overline{\delta({}_{los}v_{I,1})} \approx -0.405$ m/s and amplitude $A\left(\delta({}_{los}v_{I,1})\right) \approx 0.325$ m/s.

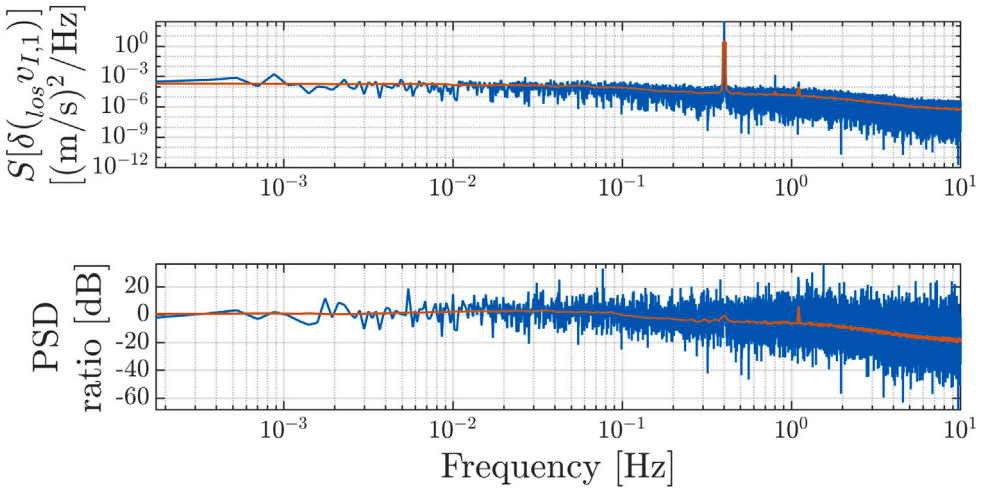

Fig. 8. Top panel: PSD of the line-of-sight velocity AKE signal. Bottom panel: ratio between the quantity in the top panel and the PSD of the line-of-sight knowledge error signal obtained using the unfiltered measurements. In red, moving averages are shown. (For interpretation of the references to color in this figure legend, the reader is referred to the web version of this article.)

visible peaks are present at 0.2 Hz, the antenna rotation fundamental frequency, and its 2nd harmonic at 0.4 Hz. The latter can be attributed to the aerodynamic torques acting on the assembly, not present in the simplified model, and which present a periodic oscillation at double the rotation frequency as the cross section exposed to the incoming atmosphere changes with this frequency.

The line-of-sight AKE signal can be mainly characterized as a sinusoid with a non-zero mean with the addition of higher frequency and lower power noise. As will be discussed in Section 4.3, this sinusoidal structure is strongly dependent on the systematic error, and this case can be considered as part of the more conservative ones.

4.2. Antenna unbalance

To study the system response to errors in the balancing body 7, a set of different simulation runs of the duration of two orbits was

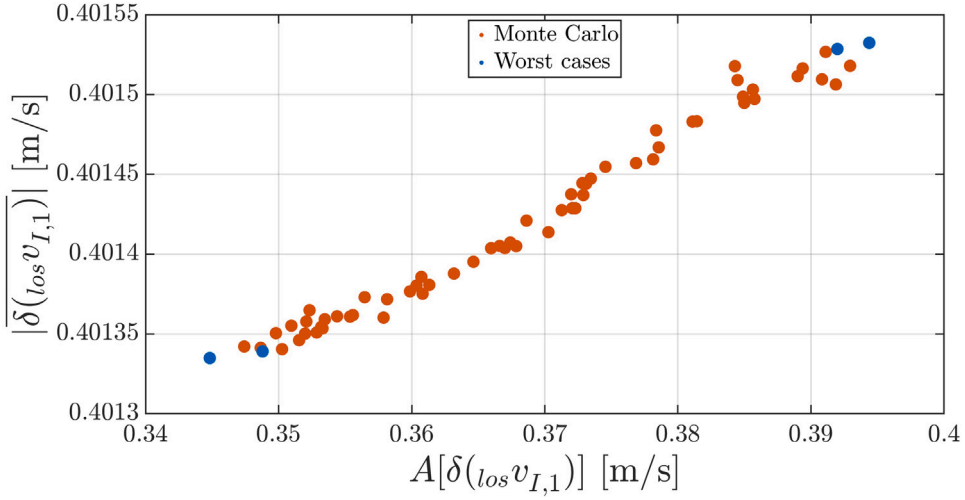

Fig. 9. Antenna unbalance analysis: amplitude vs. mean absolute bias of line-of-sight velocity AKE scatter plot. Worst cases (blue) and Monte Carlo (red) simulations. (For interpretation of the references to color in this figure legend, the reader is referred to the web version of this article.)

Table 5
Worst cases, body 7 mass and position deviations combinations.

Simulation	m_7 error	$r_{A,7}$ error
Case 1	$+\delta_m$	$+\delta_r$
Case 2	$+\delta_m$	$-\delta_r$
Case 3	$-\delta_m$	$+\delta_r$
Case 4	$-\delta_m$	$-\delta_r$

conducted, adopting the nominal case in Section 4.1 as the undisturbed case. Variations are applied to the mass m_7 and its distance from the hinge point O^A, $r_{A,7}$, with respect to the exact values to obtain perfect static and dynamic balance of body complex A. System properties that depend on these two parameters, such as inertia, are modified accordingly. Four cases in total were considered, as indicated in Table 5, with errors on mass of $\pm\delta_m = \pm 10$ g and on position of $\pm\delta_r = \pm 10$ mm. Different combinations of mass and position may produce the same static and dynamic unbalances, but the ones adopted have been chosen as conservative values if interpreted as errors during assembly of the spacecraft. Other system properties are kept the same as in the nominal simulations: nominal values are indicated in Table Appendix D.

Results for worst case and Monte Carlo analyses are shown in Fig. 9 as blue and red dots, respectively. In all cases, the line-of-sight velocity AKE signal mainly consists of a constant value (bias, $\overline{\delta({}_{los}v_{I,1})}$) plus a sinusoidal component, the amplitude of which is indicated with $A\left(\delta({}_{los}v_{I,1})\right)$. The sinusoidal component has a period of 5 s, justifiable by the fact that unbalances produce sinusoidal disturbance torques in sync with the antenna rotation. Results are presented in terms of scatter plots of amplitude vs. mean absolute bias of the line-of-sight velocity AKE signal in Fig. 9. The effect is mainly an increases in the amplitude of the sinusoidal signal of the line-of-sight velocity, obtaining higher maximum AKE in absolute value.

In the Monte Carlo campaign, errors are applied to m_7 and $r_{A,7}$ in a uniform distribution between $\pm\delta m$ and $\pm\delta r$. A total of 60 simulations are conducted, in order to obtain a confidence level of 95% as indicated in [47]. As expected, the outcomes of the simulations fall in between the worst cases.

For all cases considered the signal remains bounded between values smaller than the requirement of 1 m/s. The mean values remain roughly constant (variations of less than 1 mm/s) and amplitudes range approximately from 0.34 to 0.4 m/s. In comparison with the nominal results in Section 4.1, antenna unbalances introduce an increase of around 2 to 8 cm/s in amplitude, while practically not impacting the constant bias.

4.3. Start trackers systematic errors

The systematic errors of the star tracker play an important role in the values of the LOS velocity (${}_{los}\boldsymbol{v}_{I,1}$) AKE. The EKF is not very effective at filtering errors at lower frequencies, and these effects generate constant biases and sinusoidal signals. In order to study worst cases of maximum LOS velocity AKE, a positive or negative maximum systematic error is assumed on each of the three axis of each of the three star cameras. As this translates to a rotation of a fixed angular value $\pm\epsilon_{sys}^{max}$ on nine axes, a total of $2^9 = 512$ cases are possible. These simulations consider the maximum, worst case values over a significant statistical sample for the systematic error, as indicated in [42,45]. Other system properties are kept the same as in the nominal simulations: nominal values are indicated in Table Appendix D.

The results of the worst case analysis cluster in four distinct closely grouped clusters in Fig. 10 (blue dots). Depending on the systematic error disposition for each star camera, the signal consists of a low or high mean value with a low or high amplitude. Maximum value of AKE, for all worst cases simulated, are around 0.78 m/s, which can be also observed from Fig. 10 adding maximum values of mean and amplitude of the top right cluster.

In the Monte Carlo campaign, the systematic error of each star camera is obtained from a uniform distribution between $\pm\epsilon_{sys}^{max}$. The results are shown as red dots in Fig. 10. In general, the results fall in between or below the worst case clusters, which already identifies the star tracker as a critical component for attitude determination and pointing.

These results, in conjunction with the ones in Section 4.1, show that the AKE signal is mainly dominated by low frequency components, constant biases and sinusoids at the antenna rotation frequency (and higher harmonics, in much smaller part). Such contributions to the error can be identified and calibrated with post-processing data analysis methods, allowing for further correction of the final scientific data [8,20,24].

5. Conclusions and discussion

An AOCS simulator with an accurate model of the determination system was developed for the multibody dynamics of the WIVERN spacecraft which involves a Doppler radar with a large fast spinning antenna. In order to carry out precise assessment of the pointing, in depth modeling of the sensors and the filtering algorithm was carried out. An implementation of an Extended Kalman Filter was proposed with a simplified model of the complex multibody dynamics of the spacecraft. The ultimate goal of the study is the verification of the mission requirements

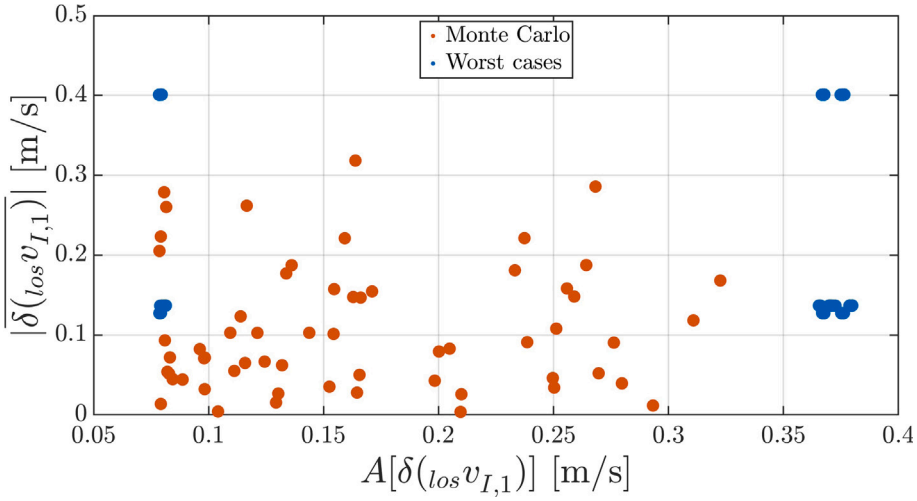

Fig. 10. Star tacker systematic error analysis: amplitude vs. mean absolute bias of line-of-sight velocity AKE scatter plot. Worst cases (blue) and Monte Carlo (red) simulations. (For interpretation of the references to color in this figure legend, the reader is referred to the web version of this article.)

that are expressed in terms of line-of-sight velocity AKE and are directly traceable to science requirements. Demonstration of such capabilities was not trivial, as studies of this kind on large spacecraft with a large conically scanning rotating antenna are a novelty in literature. Along with simulations in nominal conditions, different criticalities have been identified during the course of the simulations, in particular regarding the imperfect balancing of the antenna assembly and the star tracker accuracy, which may crucially affect the pointing determination.

Results of the simulation in nominal conditions (see Section 4.1) have highlighted that, the state of the spacecraft and its pointing can be known in order to fulfill the line-of-sight velocity AKE requirement of ± 1 m/s. An analysis in the frequency domain has further isolated different error contributions and outlined the action of the EKF in filtering out noise at higher frequencies. Mitigating high-frequency mispointing errors is a key aspect in the design of the WIVERN mission, as data-driven calibrating techniques are available for filtering out lower frequency errors [8,20,24], such as biases and periodical effects dependent on the antenna rotation.

Taking the nominal simulation as the reference case, considerations on system uncertainties have been carried out.

In Section 4.2, mass and position of body 7 were perturbed to study the effects of static and dynamic unbalance of the rotating antenna assembly, taking into consideration and error of 10 mm and 10 g on position and mass, respectively. In general, the AKE of the LOS velocity is affected by introducing a sinusoidal component in the LOS velocity signal with period equal to the antenna rotation and with amplitude dependent upon the torques generated by the unbalances.

The star tracker is a critical component of the observing system; Section 4.3 addresses the effect of systematic errors of the sensor alignment, parametrized in terms of nine free parameters. Each combination represent a measured misalignment of the attitude main body, which in turn produce different structures in the signal of the LOS velocity AKE. Four different groups were observed, with different combination of the bias and the sinusoidal component amplitude were observed.

The simulations have shown that the system is able to guarantee the desired pointing knowledge when considering realistic sets of measurement uncertainties, within the specified requirements. Additional correction method can be then used to further calibrate the mispointing error.

The developed tool is quite flexible and could be exploited for addressing further criticalities:

- Different bodies may be taken into account, such as a different antenna assembly or reaction wheels, or a different control law;
- The set of sensor may be changed, for example adopting sensor with higher errors or slower sample rates, to address the ability to fulfill the requirements with lower-end components;
- A different estimation algorithm may be adopted, such as an Unscented Kalman Filter, which may address some of the criticalities pointed out.

CRediT authorship contribution statement

Francesco Manconi: Writing – review & editing, Writing – original draft, Visualization, Validation, Software, Methodology, Investigation, Formal analysis, Data curation, Conceptualization. **Paolo Martire:** Writing – review & editing, Writing – original draft, Visualization, Validation, Software, Methodology, Investigation, Formal analysis, Data curation, Conceptualization. **Fabrizio Stesina:** Writing – review & editing, Writing – original draft, Validation, Supervision, Project administration, Methodology, Investigation, Conceptualization. **Alessandro Battaglia:** Writing – review & editing, Writing – original draft, Validation, Supervision, Resources, Project administration, Methodology, Investigation, Funding acquisition, Conceptualization.

Declaration of competing interest

The authors declare that they have no known competing financial interests or personal relationships that could have appeared to influence the work reported in this paper.

Acknowledgments

This research has been supported by the European Space Agency (ESA) under the activities “WInd VElocity Radar Nephoscope (WIVERN) Phase A Science and Requirements Consolidation Study” (ESA Contract Number RFP/3-18420/24/NL/IB/ab) and by the Italian Space Agency (ASI) project “Scientific studies for the Wind Velociy Radar Nephoscope (WIVERN) mission” (Project number: 2023-44-HH.0).

The work by Paolo Martire has been funded by the Italian Ministry of Universty and Research (MUR) as part of the PNRR-NGEU project (Ministerial Decree DM 351/2022).

The work by Franceso Manconi has been funded by the Space It Up project funded by the Italian Space Agency (ASI) and the Italian Ministry of University and Research (MUR) under contract n. 2024-5-E.0 - CUP n. I53D24000060005.

Appendix A. Nomenclature

$\textcircled{\lambda}$	Center of mass of body λ.
$\textcircled{\bullet}$	Center of mass of the spacecraft.
m_λ	Mass of body λ.
m	Mass of the spacecraft.
$\hat{\mathbf{e}}_i^j$	Axis $i = x, y, z$ of frame $\mathcal{F}^j$.
$\mathbf{r}_{i,j}$	Position vector from point O^i to O^j.
$\mathbf{v}_{I,j}$	Absolute velocity vector of point O^j.
$\mathbf{I}_i^{(\lambda)}$	Inertia dyadic of body λ (or the spacecraft, if right superscript is missing) measured about point O^i.
$\mathbf{J}_{i/j}^{(\lambda)}$	Mixed inertia dyadic of body λ, measured about points O^i and O^j.
$\mathbf{p}^{(\lambda)}$	Translational momentum of body λ (or the spacecraft, if right superscript is missing).
$\mathbf{h}_i^{(\lambda)}$	Angular momentum of body λ (or the spacecraft, if right superscript is missing) about point O^i.
$\mathbf{f}^{(\lambda)}$	Force acting on body λ (or the spacecraft, if the right superscript is missing).
$\boldsymbol{\tau}_i^{(\lambda)}$	Torque acting on body λ (or the spacecraft, if the right superscript is missing) about point O^i.
$u^{(\lambda)}$	Control torque acting on body λ about rotation axis $\hat{\mathbf{e}}_z^\lambda$.
$\boldsymbol{T}^{i,j}$	Transformation matrix from $\mathcal{F}^j$ to $\mathcal{F}^i$ coordinates.
$\mathbf{q}^{i,j}$	Quaternion describing the rotation of frame $\mathcal{F}^i$ into frame $\mathcal{F}^j$.
$\boldsymbol{\omega}^j$	Angular velocity vector of frame $\mathcal{F}^j$ about inertial frame $\mathcal{F}^I$.
$\boldsymbol{\Omega}^j$	Angular velocity vector of frame $\mathcal{F}^j$ about frame $\mathcal{F}^1$.
$\mathbf{E}$	Unit dyadic.
$\tilde{\mathbf{r}}$	3×3 skew-symmetric dyadic of vector $\mathbf{r}$.
$\boldsymbol{E}_n$	$n \times n$ identity matrix.
$\mathbf{0}_{m,n}$	$m \times n$ zero matrix. If the subscript is missing, it indicates the three-dimensional null vector.
$\delta(\ldots)$	Instantaneous knowledge error of a given variable, obtained as the subtraction of the measure/estimate from the true value.
$S[\ldots]$	Power Spectral Density (PSD) of a given variable.
$\overline{(\ldots)}$	Mean value of a given variable, averaged over its total duration.
$A(\ldots)$	Peak amplitude of a given variable with respect to the mean value over its total duration.

Appendix B. Forces and torques

B.1. Gravitational

From [21, Section 8.1], the gravitational potential of an infinitesimal mass dm can be expanded about the spacecraft's center of mass $\textcircled{\bullet}$ through a second-order Taylor expansion. The gravitational force is derived from the potential by taking its gradient. Denoting the position of dm about $\textcircled{\bullet}$ as $\mathbf{r}_{\textcircled{\bullet}}$ and the position about O^I as $\mathbf{r}_I$, the gravitational force acting on dm is given by:

$$d\mathbf{f}_{gr} = -\left[\frac{\mu}{r_{I,\textcircled{\bullet}}^2}\hat{\mathbf{e}}_z^L + \frac{\mu}{r_{I,\textcircled{\bullet}}^3}\left(\mathbf{E} - 3\hat{\mathbf{e}}_z^L\hat{\mathbf{e}}_z^L\right)\cdot\mathbf{r}_{\textcircled{\bullet}}\right]dm \tag{B.1}$$

being μ the Earth's gravitational parameter. Integrating (B.1) over any body λ and then summing all the contributions, yields:

$$\begin{aligned}\mathbf{f}_{gr}^{(\lambda)} &= \int_\lambda d\mathbf{f}_{gr} = -m_\lambda\left[\frac{\mu}{r_{I,\textcircled{\bullet}}^2}\hat{\mathbf{e}}_z^L + \frac{\mu}{r_{I,\textcircled{\bullet}}^3}\left(\mathbf{E} - 3\hat{\mathbf{e}}_z^L\hat{\mathbf{e}}_z^L\right)\cdot\mathbf{r}_{\textcircled{\bullet},\textcircled{\lambda}}\right]\\ \mathbf{f}_{gr} &= \sum_{\lambda\in B}\mathbf{f}_{gr}^{(\lambda)} = -m\frac{\mu}{r_{I,\textcircled{\bullet}}^2}\hat{\mathbf{e}}_z^L\end{aligned} \tag{B.2}$$

The gravitational torque acting on any body λ about a generic point O^i is computed as follows:

$$\begin{aligned}\boldsymbol{\tau}_{i,gr}^{(\lambda)} &= \int_\lambda \mathbf{r}_i \times d\mathbf{f}_{gr}\\ &= -\int_\lambda \mathbf{r}_i \times \left[\frac{\mu}{r_{I,\textcircled{\bullet}}^2}\hat{\mathbf{e}}_z^L + \frac{\mu}{r_{I,\textcircled{\bullet}}^3}\left(\mathbf{E} - 3\hat{\mathbf{e}}_z^L\hat{\mathbf{e}}_z^L\right)\cdot\left(\mathbf{r}_{\textcircled{\bullet},i} + \mathbf{r}_i\right)\right]dm\end{aligned} \tag{B.3}$$

Making use of the relation:

$$\begin{aligned}\mathbf{a}\times[(\mathbf{bb})\cdot\mathbf{c}] &= \mathbf{a}\times[\mathbf{b}(\mathbf{c}\cdot\mathbf{b})] = -\mathbf{b}\times[\mathbf{a}(\mathbf{c}\cdot\mathbf{b})]\\ &= \mathbf{b}\times[(k\mathbf{E} - \mathbf{ac})\cdot\mathbf{b}]\end{aligned} \tag{B.4}$$

being $\mathbf{a}$, $\mathbf{b}$ and $\mathbf{c}$ generic vectors and k any scalar, the integration of (B.3) yields:

$$\begin{aligned}\boldsymbol{\tau}_{i,gr}^{(\lambda)} = -m_\lambda\mathbf{r}_{i,\textcircled{\lambda}}\times&\left(\frac{\mu}{r_{I,\textcircled{\bullet}}^2}\hat{\mathbf{e}}_z^L + \frac{\mu}{r_{I,\textcircled{\bullet}}^3}\mathbf{r}_{\textcircled{\bullet},i}\right) + 3\frac{\mu}{r_{I,\textcircled{\bullet}}^3}\hat{\mathbf{e}}_z^L\\ &\times\left(\mathbf{I}_i^{(\lambda)} - m_\lambda\mathbf{r}_{i,\textcircled{\lambda}}\mathbf{r}_{\textcircled{\bullet},i}\right)\cdot\hat{\mathbf{e}}_z^L\end{aligned} \tag{B.5}$$

The total gravitational torque acting on the spacecraft, $\boldsymbol{\tau}_{1,gr}$, is obtained by referring (B.5) about point O^1 and then summing all the contributions from each body:

$$\boldsymbol{\tau}_{1,gr} = \sum_{\lambda\in B}\boldsymbol{\tau}_{1,gr}^{(\lambda)} = \mathbf{r}_{1,\textcircled{\bullet}}\times\mathbf{f}_{gr} + 3\frac{\mu}{r_{I,\textcircled{\bullet}}^3}\hat{\mathbf{e}}_z^L\times\mathbf{I}_{\textcircled{\bullet}}\cdot\hat{\mathbf{e}}_z^L \tag{B.6}$$

where we implicitly made use of the parallel axis theorem:

$$\mathbf{I}_{\textcircled{\bullet}} = \mathbf{I}_1 - m\left[\left(\mathbf{r}_{1,\textcircled{\bullet}}\cdot\mathbf{r}_{1,\textcircled{\bullet}}\right)\mathbf{E} - \mathbf{r}_{1,\textcircled{\bullet}}\mathbf{r}_{1,\textcircled{\bullet}}\right] \tag{B.7}$$

B.2. Aerodynamic

The aerodynamic torques are computed by assuming the air molecules move in straight lines (i.e., free molecular flow regime) and transfer all their momentum to the spacecraft when hitting the surface. The relative velocity between any exposed point of the surface and the air molecules is assumed equal to the velocity of $\textcircled{\bullet}$, implying that the component of relative velocity associated with rotational motion is being neglected. Following this approach, outlined in more detail in [21, Section 8.2], the force acting on the infinitesimal element of the surface $d\sigma$ is:

$$d\mathbf{f}_{ae} = \rho_a v_{I,\textcircled{\bullet}}^2\hat{\mathbf{e}}_v\left(\hat{\mathbf{e}}_v\cdot\mathbf{n}\right)d\sigma \tag{B.8}$$

meaning that the force acting on $d\sigma$ is given by the momentum flux of air molecules entering the surface. In (B.8), ρ_a represents the atmospheric density, $\hat{\mathbf{e}}_v$ is the unit vector parallel to $\mathbf{v}_{I,\textcircled{\bullet}}$, while $\mathbf{n}$ is the inward normal to the surface. Introducing the Heaviside step function $H(x)$ to account only for the portions of the surface exposed to the incoming flow, the aerodynamic torque acting on body $\lambda \in \{1, 7, 8\}$ (i.e., bodies with external surface exposed to the flow) about any point O^i is:

$$\begin{aligned}\boldsymbol{\tau}_{i,ae}^{(\lambda)} &= \int_{\sigma(\lambda)} H\left(\hat{\mathbf{e}}_v\cdot\mathbf{n}\right)\mathbf{r}_i\times d\mathbf{f}_{ae}\\ &= \rho_a v_{I,\textcircled{\bullet}}^2\int_{\sigma(\lambda)} H\left(\hat{\mathbf{e}}_v\cdot\mathbf{n}\right)\left(\hat{\mathbf{e}}_v\cdot\mathbf{n}\right)\mathbf{r}_i\,d\sigma\times\hat{\mathbf{e}}_v\end{aligned} \tag{B.9}$$

being $\sigma(\lambda)$ the surface of body λ.

Appendix C. Simplified spacecraft dynamics

The dynamics model required for the Sliding Mode Control and the Extended Kalman Filter involves the explicit derivation of time derivatives for the translational and angular momenta. As these equations are formulated in terms of vectors and dyadics, it is essential to introduce

Table D.6
Antenna assembly configuration parameters.

Antenna assembly A			
Mass	m_A	68.831	kg
Inertia	${}^{A}\boldsymbol{I}_{A}^{(A)}$	$\begin{bmatrix} 171.664 & 0 & 0 \\ 0 & 171.664 & 0 \\ 0 & 0 & 64.115 \end{bmatrix}$	kg m^2
Rotation axis	${}^{1}_{z}\hat{\boldsymbol{e}}^{A}$	$\{0 \quad 0 \quad 1\}^T$	
O^A position	${}^{1}\boldsymbol{r}_{1,A}$	$\{0 \quad 0 \quad -1.375\}^T$	m
CoM position	${}^{A}\boldsymbol{r}_{A,\textcircled{A}}$	$\{0 \quad 0 \quad -1.25\}^T$	m
Balancing mass 7			
Mass	m_7	11.719	kg
Inertia	${}^{A}\boldsymbol{I}_{A}^{(7)}$	$\begin{bmatrix} 1.294\times10^{-1} & 0 & -1.0051 \\ 0 & 9.672 & 0 \\ -1.0051 & 0 & 9.566 \end{bmatrix}$	kg m^2
CoM position	${}^{A}\boldsymbol{r}_{A,7}$	$\{-9.023\times10^{-1} \quad 0 \quad -9.505\times10^{-2}\}^T$	m
Antenna reflector 8			
Mass	m_8	57.112	kg
Inertia	${}^{A}\boldsymbol{I}_{A}^{(8)}$	$\begin{bmatrix} 171.535 & 0 & 1.0051 \\ 0 & 161.992 & 0 \\ 1.0051 & 0 & 54.549 \end{bmatrix}$	kg m^2
O^8 position	${}^{A}\boldsymbol{r}_{A,8}$	$[0, 0, -1.25]^T$	m
CoM position	${}^{A}\boldsymbol{r}_{8,\textcircled{8}}$	$\{1.852\times10^{-1} \quad 0 \quad -2.37\times10^{-1}\}^T$	m

Table D.7
Platform configuration parameters. Wheels specifications are reported in [48].

Body 1			
Mass	m_1	996.2	kg
Inertia	${}^{1}\boldsymbol{I}_{1}^{(1)}$	diag(1175, 1528, 893.2)	kg m^2
Wheels $\lambda \in \{2,\dots,5\}$ (Honeywell HR14-50)			
Mass	m_λ	8.5	kg
Rotation axis	${}^{1}_{z}\hat{\boldsymbol{e}}^{2}$	$\{0.5 \quad 0.5 \quad \sqrt{2}/2\}^T$	
Rotation axis	${}^{1}_{z}\hat{\boldsymbol{e}}^{3}$	$\{-0.5 \quad 0.5 \quad \sqrt{2}/2\}^T$	
Rotation axis	${}^{1}_{z}\hat{\boldsymbol{e}}^{4}$	$\{-0.5 \quad -0.5 \quad \sqrt{2}/2\}^T$	
Rotation axis	${}^{1}_{z}\hat{\boldsymbol{e}}^{5}$	$\{0.5 \quad -0.5 \quad \sqrt{2}/2\}^T$	
O^2 position	${}^{1}\boldsymbol{r}_{1,2}$	$\{0.55 \quad 0.325 \quad 0\}^T$	m
O^3 position	${}^{1}\boldsymbol{r}_{1,3}$	$\{-0.55 \quad 0.325 \quad 0\}^T$	m
O^4 position	${}^{1}\boldsymbol{r}_{1,4}$	$\{-0.55 \quad -0.325 \quad 0\}^T$	m
O^5 position	${}^{1}\boldsymbol{r}_{1,5}$	$\{0.55 \quad -0.325 \quad 0\}^T$	m
CoM position	${}^{\lambda}\boldsymbol{r}_{\lambda,\textcircled{\lambda}}$	$\{4.121\times10^{-1} \quad 0 \quad -9.946\times10^{-6}\}^T$	μm
Inertia	${}^{\lambda}\boldsymbol{I}_{\lambda}^{(\lambda)}$	$\begin{bmatrix} 4.176\times10^{-2} & 0 & 9.1\times10^{-7} \\ 0 & 4.176\times10^{-2} & 0 \\ 9.1\times10^{-7} & 0 & 7.947\times10^{-2} \end{bmatrix}$	kg m^2
Max speed		±6000	rpm
Max torque		0.2	N m
Wheel 6 (Honeywell HR16-100)			
Mass	m_6	12	kg
Inertia	${}^{6}\boldsymbol{I}_{6}^{(6)}$	$\begin{bmatrix} 8.243\times10^{-2} & 0 & 1.54\times10^{-6} \\ 0 & 8.243\times10^{-2} & 0 \\ 1.54\times10^{-6} & 0 & 1.592\times10^{-1} \end{bmatrix}$	kg m^2
Rotation axis	${}^{1}_{z}\hat{\boldsymbol{e}}^{6}$	$\{0 \quad 0 \quad 1\}^T$	
O^6 position	${}^{1}\boldsymbol{r}_{1,6}$	$\{0 \quad 0 \quad -0.6875\}^T$	m
CoM position	${}^{\lambda}\boldsymbol{r}_{\lambda,\textcircled{\lambda}}$	$\{4\times10^{-1} \quad 0 \quad -8.028\times10^{-6}\}^T$	μm
Max speed		±6000	rpm
Max torque		0.2	N m

the differentiation identities from vector calculus. Given a frame $\mathcal{F}^j$ rotating with angular velocity $\boldsymbol{\omega}^{i,j}$ about another frame $\mathcal{F}^i$, the time derivative with respect to $\mathcal{F}^i$ of any vector $\mathbf{a}$ or dyadic $\mathbf{D}$ expressed in $\mathcal{F}^j$ is:

$$\begin{aligned} {}^{i}\frac{d}{dt}\mathbf{a} &= \dot{\mathbf{a}} + \boldsymbol{\omega}^{i,j} \times \mathbf{a} \\ {}^{i}\frac{d}{dt}\mathbf{D} &= \dot{\mathbf{D}} + \boldsymbol{\omega}^{i,j} \times \mathbf{D} - \mathbf{D} \times \boldsymbol{\omega}^{i,j} \end{aligned} \tag{C.1}$$

Consistent with the approach taken elsewhere in the article, we simplify the notation by denoting the angular velocity of any frame $\mathcal{F}^j$ as $\boldsymbol{\omega}^j$ if referred to inertial frame $\mathcal{F}^I$, and $\boldsymbol{\Omega}^j$ if referred to body frame $\mathcal{F}^1$.

In the simplified model derived in this section, the wheels and the antenna assembly are assumed perfectly balanced. Moreover, it is assumed that both aerodynamic and gravity-gradient-induced external torques are absent. Based on the balancing assumptions of the simplified model, it is convenient to express all the CoM displacement vectors and inertia dyadics in (1), (2) and (5) in $\mathcal{F}^1$, as they have constant components with respect to this frame. By substituting (2) into (8) and carrying out the derivation through (C.1), (8) expands as follows:

$$\begin{aligned} {}^{I}\frac{d}{dt}\mathbf{h}_1 = {} & m\left(\boldsymbol{\omega}^1 \times \mathbf{r}_{1,\textcircled{\bullet}}\right) \times \mathbf{v}_{I,1} + m\mathbf{r}_{1,\textcircled{\bullet}} \times \dot{\mathbf{v}}_{I,1} \\ & + \left(\boldsymbol{\omega}^1 \times \mathbf{I}_1 - \mathbf{I}_1 \times \boldsymbol{\omega}^1\right) \cdot \boldsymbol{\omega}^1 + \mathbf{I}_1 \cdot \dot{\boldsymbol{\omega}}^1 \\ & + \sum_{\lambda \in W} \left[\left(\boldsymbol{\omega}^1 \times \mathbf{I}_\lambda^{(\lambda)} - \mathbf{I}_\lambda^{(\lambda)} \times \boldsymbol{\omega}^1\right) \cdot \boldsymbol{\Omega}^\lambda + \mathbf{I}_\lambda^{(\lambda)} \cdot \left(\dot{\boldsymbol{\Omega}}^\lambda + \boldsymbol{\omega}^1 \times \boldsymbol{\Omega}^\lambda\right)\right] \\ & + \left[\boldsymbol{\omega}^1 \times \left(\mathbf{J}_{A/1}^{(A)} + \mathbf{I}_A^{(A)}\right) - \left(\mathbf{J}_{A/1}^{(A)} + \mathbf{I}_A^{(A)}\right) \times \boldsymbol{\omega}^1\right] \cdot \boldsymbol{\Omega}^A \\ & + \left(\mathbf{J}_{A/1}^{(A)} + \mathbf{I}_A^{(A)}\right) \cdot \left(\dot{\boldsymbol{\Omega}}^A + \boldsymbol{\omega}^1 \times \boldsymbol{\Omega}^A\right) = -\mathbf{v}_{I,1} \times \mathbf{p} + \mathbf{r}_{1,\textcircled{\bullet}} \times \mathbf{f}_{gr} \end{aligned} \tag{C.2}$$

where relations $\mathbf{r}_{\lambda,\textcircled{\lambda}} = \mathbf{0}$ and $\mathbf{J}_{\lambda/1}^{(\lambda)} = \mathbf{0}$ $(\forall \lambda \in W)$, derived from the assumption of balanced wheels, have been introduced in (2) prior to substitution. It can be observed that all terms in the form $(\mathbf{D} \times \mathbf{a}) \cdot \mathbf{a}$ are null, as the operation implies the cross product between two identical vectors. Moreover, it may be noted that $(\mathbf{D} \times \mathbf{a}) \cdot \mathbf{b} = \mathbf{D} \cdot (\mathbf{a} \times \mathbf{b})$ which allows to simplify further terms. As a further step, it is necessary to derive relationships for $\mathbf{p}$, $\dot{\mathbf{v}}_{I,1}$ and $\dot{\boldsymbol{\Omega}}^\lambda$. The expression for $\mathbf{p}$ is obtained by introducing the simplified model assumption $\mathbf{r}_{\lambda,\textcircled{\lambda}} = \mathbf{0}$ $(\forall \lambda \in W)$ and $\mathbf{r}_{A,\textcircled{A}} \parallel \hat{\mathbf{e}}_z^A$ into (1):

$$\mathbf{p} = m\left(\mathbf{v}_{I,1} - \mathbf{r}_{1,\textcircled{\bullet}} \times \boldsymbol{\omega}^1\right) \tag{C.3}$$

The derivative of $\mathbf{p}$, given by (7), is expanded through (C.1) as follows:

$${}^{I}\frac{d}{dt}\mathbf{p} = m\left[\dot{\mathbf{v}}_{I,1} - \left(\boldsymbol{\omega}^1 \times \mathbf{r}_{1,\textcircled{\bullet}}\right) \times \boldsymbol{\omega}^1 - \mathbf{r}_{1,\textcircled{\bullet}} \times \dot{\boldsymbol{\omega}}^1\right] = \mathbf{f}_{gr} \tag{C.4}$$

from which we obtain the expression for $\dot{\mathbf{v}}_{I,1}$:

$$\dot{\mathbf{v}}_{I,1} = \left(\boldsymbol{\omega}^1 \times \mathbf{r}_{1,\textcircled{\bullet}}\right) \times \boldsymbol{\omega}^1 + \mathbf{r}_{1,\textcircled{\bullet}} \times \dot{\boldsymbol{\omega}}^1 + \frac{\mathbf{f}_{gr}}{m} \tag{C.5}$$

The equation for $\dot{\boldsymbol{\Omega}}^\lambda$ $(\lambda \in W)$ can be derived by writing the projected angular momentum Eqs. (5) and (9) for a perfectly balanced cylindrical rotor. Introducing the inertia dyadic relation for a cylindrical rotor about its principal axes of inertia:

$$\begin{aligned} \mathbf{I}_\lambda^{(\lambda)} &= \left\{\hat{\mathbf{e}}^\lambda\right\}^T {}^{\lambda}\boldsymbol{I}_\lambda^{(\lambda)} \left\{\hat{\mathbf{e}}^\lambda\right\} \\ &= I_{\lambda,tr}^{(\lambda)} \hat{\mathbf{e}}_x^\lambda \hat{\mathbf{e}}_x^\lambda + I_{\lambda,tr}^{(\lambda)} \hat{\mathbf{e}}_y^\lambda \hat{\mathbf{e}}_y^\lambda + I_{\lambda,rot}^{(\lambda)} \hat{\mathbf{e}}_z^\lambda \hat{\mathbf{e}}_z^\lambda \\ &= I_{\lambda,tr}^{(\lambda)} \mathbf{E} + \left(I_{\lambda,rot}^{(\lambda)} - I_{\lambda,tr}^{(\lambda)}\right) \hat{\mathbf{e}}_z^\lambda \hat{\mathbf{e}}_z^\lambda \end{aligned} \tag{C.6}$$

and performing the appropriate algebraic steps and simplifications, the equation of motion (9) yields:

$$\mathbf{I}_\lambda^{(\lambda)} \cdot \dot{\boldsymbol{\Omega}}^\lambda = I_{\lambda,rot}^{(\lambda)} \dot{\Omega}^\lambda \hat{\mathbf{e}}_z^\lambda = \left(u^{(\lambda)} - I_{\lambda,rot}^{(\lambda)} \hat{\mathbf{e}}_z^\lambda \cdot \dot{\boldsymbol{\omega}}^1\right) \hat{\mathbf{e}}_z^\lambda \tag{C.7}$$

where $u^{(\lambda)}$ is the control torque about $\hat{\mathbf{e}}_z^\lambda$ exerted by the motor on the λth wheel. Substituting (C.3), (C.5) and (C.7) into (C.2), and performing

Table D.8
Simulation parameters. Initial conditions for the position and velocity of ◓ refer to a circular orbit of 500 km, with an inclination of 97.42°, argument of perigee of 90°, and RAAN and mean anomaly set to zero.

Simulation period		11400	s
Time step		5×10^{-4}	s
Initial conditions			
Quaternion from $\mathcal{F}^I$ to $\mathcal{F}^1$	$\mathbf{q}^{I,1}$	$\{0.8642 \quad -5.6\times10^{-2} \quad -3.23\times10^{-2} \quad 0.5\}^T$	
Quaternion from $\mathcal{F}^1$ to $\mathcal{F}^2$	$\mathbf{q}^{1,2}$	$\{8.536 \quad -1.464 \quad 3.536 \quad 3.536\}^T \times 10^{-1}$	
Quaternion from $\mathcal{F}^1$ to $\mathcal{F}^3$	$\mathbf{q}^{1,3}$	$\{3.536 \quad -3.536 \quad 1.464 \quad 8.536\}^T \times 10^{-1}$	
Quaternion from $\mathcal{F}^1$ to $\mathcal{F}^4$	$\mathbf{q}^{1,4}$	$\{3.536 \quad 3.536 \quad 1.464 \quad -8.536\}^T \times 10^{-1}$	
Quaternion from $\mathcal{F}^1$ to $\mathcal{F}^5$	$\mathbf{q}^{1,5}$	$\{8.536 \quad 1.464 \quad 3.536 \quad -3.536\}^T \times 10^{-1}$	
Quaternion from $\mathcal{F}^1$ to $\mathcal{F}^6$	$\mathbf{q}^{1,6}$	$\{1 \quad 0 \quad 0 \quad 0\}^T$	
Quaternion from $\mathcal{F}^1$ to $\mathcal{F}^A$	$\mathbf{q}^{1,A}$	$\{1 \quad 0 \quad 0 \quad 0\}^T$	
Absolute ang. velocity of $\mathcal{F}^1$	${}^1\boldsymbol{\omega}^1$	$\{0 \quad 0 \quad 0\}^T$	rad/s
Absolute ang. velocity of $\mathcal{F}^\lambda$ about $\hat{\mathbf{e}}_z^\lambda$ ($\lambda \in W$)	${}^\lambda_z\omega^\lambda$	0	rad/s
Absolute ang. velocity of $\mathcal{F}^A$ about $\hat{\mathbf{e}}_z^A$	${}^A_z\omega^A$	$2\pi/5$	rad/s
S/C absolute position	${}^1\boldsymbol{r}_{I,◓}$	$\{0 \quad 0 \quad 6.878\times10^6\}^T$	m
S/C absolute velocity	${}^1\boldsymbol{v}_{I,◓}$	$\{7.613\times10^3 \quad 0 \quad 0\}^T$	m/s
Controller parameters			
Control frequency		5	Hz
Control gain matrix	$\boldsymbol{K}_1$	$\begin{bmatrix} 0.6\boldsymbol{E} & 0 \\ 0 & 5 \end{bmatrix}$	
Control gain matrix	$\boldsymbol{K}_2$	$\begin{bmatrix} 0.1\boldsymbol{E} & 0 \\ 0 & 3 \end{bmatrix}$	
tanh slope	η	1	

simplifications of null and equal and opposite terms, yields:

$$\begin{aligned}
&\left(\mathbf{I}_1 + m\tilde{\mathbf{r}}_{1,◓}\cdot\tilde{\mathbf{r}}_{1,◓} - \sum_{\lambda\in W} I^{(\lambda)}_{\lambda,rot}\hat{\mathbf{e}}^\lambda_z\hat{\mathbf{e}}^\lambda_z\right)\cdot\dot{\boldsymbol{\omega}}^1 + \left[\left(\mathbf{J}^{(A)}_{1/A} + \mathbf{I}^{(A)}_A\right)\cdot\hat{\mathbf{e}}^A_z\right]\dot{\Omega}^A \\
&= -m\mathbf{r}_{1,◓}\times\left[\left(\boldsymbol{\omega}^1\times\mathbf{r}_{1,◓}\right)\times\boldsymbol{\omega}^1\right] - \tilde{\boldsymbol{\omega}}^1\cdot\mathbf{I}_1\cdot\boldsymbol{\omega}^1 - \sum_{\lambda\in W}\tilde{\boldsymbol{\omega}}^1\cdot I^{(\lambda)}_{\lambda,rot}\Omega^\lambda\hat{\mathbf{e}}^\lambda_z \\
&\quad - \tilde{\boldsymbol{\omega}}^1\cdot\left(\mathbf{J}^{(A)}_{1/A} + \mathbf{I}^{(A)}_A\right)\cdot\Omega^A\hat{\mathbf{e}}^A_z - \sum_{\lambda\in W}u^{(\lambda)}\hat{\mathbf{e}}^\lambda_z \triangleq \mathbf{g}^{(B)}\left(\boldsymbol{\omega}^1,\Omega^2,\ldots,\Omega^A\right) - \mathbf{u}^{(W)}
\end{aligned} \tag{C.8}$$

where:

$$\begin{aligned}
\mathbf{g}^{(B)} &\triangleq -m\mathbf{r}_{1,◓}\times\left[\left(\boldsymbol{\omega}^1\times\mathbf{r}_{1,◓}\right)\times\boldsymbol{\omega}^1\right] - \tilde{\boldsymbol{\omega}}^1\cdot\mathbf{I}_1\cdot\boldsymbol{\omega}^1 \\
&\quad - \sum_{\lambda\in W}\tilde{\boldsymbol{\omega}}^1\cdot I^{(\lambda)}_{\lambda,rot}\Omega^\lambda\hat{\mathbf{e}}^\lambda_z - \tilde{\boldsymbol{\omega}}^1\cdot\left(\mathbf{J}^{(A)}_{1/A} + \mathbf{I}^{(A)}_A\right)\cdot\Omega^A\hat{\mathbf{e}}^A_z \\
\mathbf{u}^{(W)} &\triangleq \sum_{\lambda\in W}u^{(\lambda)}\hat{\mathbf{e}}^\lambda_z
\end{aligned} \tag{C.9}$$

Similarly, the equation of motion for the antenna assembly is derived by expanding (9):

$$\begin{aligned}
\hat{\mathbf{e}}^A_z\cdot\frac{^I d}{dt}\mathbf{h}^{(A)}_A &= \hat{\mathbf{e}}^A_z\cdot\left\{m_A\left(\boldsymbol{\omega}^1\times\mathbf{r}_{A,\textcircled{A}}\right)\times\mathbf{v}_{I,1} + m_A\mathbf{r}_{A,\textcircled{A}}\times\dot{\mathbf{v}}_{I,1}\right. \\
&\quad + \left[\boldsymbol{\omega}^1\times\left(\mathbf{J}^{(A)}_{1/A} + \mathbf{I}^{(A)}_A\right) - \left(\mathbf{J}^{(A)}_{1/A} + \mathbf{I}^{(A)}_A\right)\times\boldsymbol{\omega}^1\right]\cdot\boldsymbol{\omega}^1 \\
&\quad + \left(\mathbf{J}^{(A)}_{1/A} + \mathbf{I}^{(A)}_A\right)\cdot\dot{\boldsymbol{\omega}}^1 + \left(\boldsymbol{\omega}^1\times\mathbf{I}^{(A)}_A - \mathbf{I}^{(A)}_A\times\boldsymbol{\omega}^1\right)\cdot\boldsymbol{\Omega}^A \\
&\quad \left. + \mathbf{I}^{(A)}_A\cdot\left(\dot{\boldsymbol{\Omega}}^A + \boldsymbol{\omega}^1\times\boldsymbol{\Omega}^A\right)\right\} \\
&= \hat{\mathbf{e}}^A_z\cdot\left\{-\mathbf{v}_{I,A}\times\mathbf{p}^{(A)} + \mathbf{r}_{A,\textcircled{A}}\times\mathbf{f}^{(A)}_{gr} + \mathbf{u}^{(A)}\right\}
\end{aligned} \tag{C.10}$$

Introducing the antenna assembly balancing assumptions (i.e., $\mathbf{r}_{A,\textcircled{A}} \parallel \hat{\mathbf{e}}^A_z$) in (4), yields:

$$\mathbf{p}^{(A)} = \left(m_A\mathbf{v}_{I,A} - m_A\mathbf{r}_{A,\textcircled{A}}\times\boldsymbol{\omega}^1\right) \tag{C.11}$$

which can be replaced in (C.10). The balancing assumption also permits simplifications of further terms, as:

$$\hat{\mathbf{e}}^A_z\cdot\left(\mathbf{r}_{A,\textcircled{A}}\times\mathbf{a}\right) = \left(\hat{\mathbf{e}}^A_z\times\mathbf{r}_{A,\textcircled{A}}\right)\cdot\mathbf{a} = \mathbf{0}$$

being $\mathbf{a}$ a generic vector. Furthermore, we substitute:

$$\mathbf{v}_{I,1} = \mathbf{v}_{I,A} - \boldsymbol{\omega}^1\times\mathbf{r}_{1,A}$$

to allow simplification of $\mathbf{v}_{I,A}$. By carrying out the cited substitutions and simplifications, (C.10) rewrites as:

$$\begin{aligned}
&\left[\hat{\mathbf{e}}^A_z\cdot\left(\mathbf{J}^{(A)}_{1/A} + \mathbf{I}^{(A)}_A\right)\right]\cdot\dot{\boldsymbol{\omega}}^1 + \left(\hat{\mathbf{e}}^A_z\cdot\mathbf{I}^{(A)}_A\cdot\hat{\mathbf{e}}^A_z\right)\dot{\Omega}^A \\
&= \hat{\mathbf{e}}^A_z\cdot\left\{m_A\left(\boldsymbol{\omega}^1\times\mathbf{r}_{A,\textcircled{A}}\right)\times\left(\boldsymbol{\omega}^1\times\mathbf{r}_{1,A}\right)\right. \\
&\quad \left. - \tilde{\boldsymbol{\omega}}^1\cdot\left(\mathbf{J}^{(A)}_{1/A} + \mathbf{I}^{(A)}_A\right)\cdot\boldsymbol{\omega}^1 - \tilde{\boldsymbol{\omega}}^1\cdot\mathbf{I}^{(A)}_A\cdot\Omega^A\hat{\mathbf{e}}^z_z + \mathbf{u}^{(A)}\right\} \\
&\triangleq g^{(A)}\left(\boldsymbol{\omega}^1,\Omega^A\right) + u^{(A)}
\end{aligned} \tag{C.12}$$

where:

$$\begin{aligned}
g^{(A)} &\triangleq \hat{\mathbf{e}}^A_z\cdot\left\{m_A\left(\boldsymbol{\omega}^1\times\mathbf{r}_{A,\textcircled{A}}\right)\times\left(\boldsymbol{\omega}^1\times\mathbf{r}_{1,A}\right)\right. \\
&\quad \left. -\tilde{\boldsymbol{\omega}}^1\cdot\left(\mathbf{J}^{(A)}_{1/A} + \mathbf{I}^{(A)}_A\right)\cdot\boldsymbol{\omega}^1 - \tilde{\boldsymbol{\omega}}^1\cdot\mathbf{I}^{(A)}_A\cdot\Omega^A\hat{\mathbf{e}}^z_z\right\} \\
u^{(A)} &\triangleq \hat{\mathbf{e}}^A_z\cdot\mathbf{u}^{(A)}
\end{aligned} \tag{C.13}$$

Eqs. (C.8) and (C.12) can be formulated in matrix form, by defining the system matrix (beginning of the next page) and, through definitions (C.9) and (C.13), the column matrices:

$$\dot{\boldsymbol{z}} \triangleq \begin{Bmatrix} {}^1\dot{\boldsymbol{\omega}}^1 \\ \dot{\Omega}^A \end{Bmatrix} \qquad \boldsymbol{g} \triangleq \begin{Bmatrix} \boldsymbol{g}^{(B)} \\ \boldsymbol{g}^{(A)} \end{Bmatrix} \qquad \boldsymbol{u} \triangleq \begin{Bmatrix} \boldsymbol{u}^{(W)} \\ -u^{(A)} \end{Bmatrix} \tag{C.14}$$

thus obtaining the matrix Eq. (17).

$$\boldsymbol{M} \triangleq \begin{bmatrix} {}^{1}\boldsymbol{I}_{1} + m\,{}^{1}\tilde{\boldsymbol{r}}_{1,\bullet}\,{}^{1}\tilde{\boldsymbol{r}}_{1,\bullet} - \sum_{\lambda\in\mathcal{W}} I^{(\lambda)}_{\lambda,rot}\,{}^{1}\hat{\boldsymbol{e}}^{\lambda}_{z}\left({}^{1}\hat{\boldsymbol{e}}^{\lambda}_{z}\right)^{T} & \left({}^{1}\boldsymbol{J}^{(A)}_{A/1} + {}^{1}\boldsymbol{I}^{(A)}_{A}\right){}^{1}\hat{\boldsymbol{e}}^{A}_{z} \\ \left({}^{1}\hat{\boldsymbol{e}}^{A}_{z}\right)^{T}\left({}^{1}\boldsymbol{J}^{(A)}_{1/A} + {}^{1}\boldsymbol{I}^{(A)}_{A}\right) & \left({}^{1}\hat{\boldsymbol{e}}^{A}_{z}\right)^{T}{}^{1}\boldsymbol{I}^{(A)}_{A}\,{}^{1}\hat{\boldsymbol{e}}^{A}_{z} \end{bmatrix} \tag{C.15}$$

Appendix D. Simulation parameters

See Tables D.6–D.8

References

[1] S. Bidwell, G. Flaming, J. Durning, E. Smith, The global precipitation measurement (GPM) microwave imager (GMI) instrument: role, performance, and status, in: Proceedings. 2005 IEEE International Geoscience and Remote Sensing Symposium, 2005. IGARSS '05., Vol. 1, 2005, p. 4, http://dx.doi.org/10.1109/IGARSS.2005.1526109.

[2] O.S. Alvarez-Salazar, Pointing architecture of SMAP's large spinning antenna, in: AIAA Guidance, Navigation, and Control (GNC) Conference, 2013, p. 4560.

[3] F. Vanin, P. Laberinti, C. Donlon, B. Fiorelli, I. Barat, M.P. Sole, M. Palladino, P. Eggers, T. Rudolph, C. Galeazzi, Copernicus imaging microwave radiometer (CIMR): System aspects and technological challenges, in: IGARSS 2020 - 2020 IEEE International Geoscience and Remote Sensing Symposium, 2020, pp. 6535–6538, http://dx.doi.org/10.1109/IGARSS39084.2020.9324259.

[4] E. Rodríguez, M. Bourassa, D. Chelton, J.T. Farrar, D. Long, D. Perkovic-Martin, R. Samelson, The winds and currents mission concept, Front. Mar. Sci. 6 (2019) http://dx.doi.org/10.3389/fmars.2019.00438, URL https://www.frontiersin.org/journals/marine-science/articles/10.3389/fmars.2019.00438.

[5] A. Wineteer, D. Perkovic-Martin, R. Monje, E. Rodríguez, T. Gál, N. Niamsuwan, F. Nicaise, K. Srinivasan, C. Baldi, N. Majurec, B. Stiles, Measuring winds and currents with Ka-Band Doppler scatterometry: An airborne implementation and progress towards a spaceborne mission, Remote. Sens. 12 (6) (2020) http://dx.doi.org/10.3390/rs12061021, URL https://www.mdpi.com/2072-4292/12/6/1021.

[6] A.J. Illingworth, A. Battaglia, J. Bradford, M. Forsythe, P. Joe, P. Kollias, K. Lean, M. Lori, J.-F. Mahfouf, S. Melo, R. Midthassel, Y. Munro, J. Nicol, R. Potthast, M. Rennie, T.H.M. Stein, S. Tanelli, F. Tridon, C.J. Walden, M. Wolde, WIVERN: A new satellite concept to provide global in-cloud winds, precipitation, and cloud properties, BAMS 99 (8) (2018) 1669–1687, http://dx.doi.org/10.1175/BAMS-D-16-0047.1.

[7] ESA, WIVERN Report for Assessment, Tech. Rep., ESA-EOPSM-WIVE-RP-4375, 2023, URL https://atpi.eventsair.com/ucm2023/ucm-doc.

[8] A. Battaglia, P. Martire, E. Caubet, L. Phalippou, F. Stesina, P. Kollias, A. Illingworth, Observation error analysis for the WInd velocity radar nephoscope W-band Doppler conically scanning spaceborne radar via end-to-end simulations, Atmos. Meas. Tech. 15 (9) (2022) 3011–3030, http://dx.doi.org/10.5194/amt-15-3011-2022, URL https://amt.copernicus.org/articles/15/3011/2022/.

[9] F. Tridon, A. Battaglia, A. Rizik, F.E. Scarsi, A. Illingworth, Filling the gap of wind observations inside tropical cyclones, Earth Space Sci. 10 (11) (2023) e2023EA003099, http://dx.doi.org/10.1029/2023EA003099.

[10] F. Ardhuin, P. Brandt, L. Gaultier, C. Donlon, A. Battaglia, F. Boy, T. Casal, B. Chapron, F. Collard, S. Cravatte, et al., SKIM, a candidate satellite mission exploring global ocean currents and waves, Front. Mar. Sci. 6 (2019) 209.

[11] H. Torres, A. Wineteer, P. Klein, T. Lee, J. Wang, E. Rodriguez, D. Menemenlis, H. Zhang, Anticipated capabilities of the ODYSEA wind and current mission concept to estimate wind work at the air–sea interface, Remote. Sens. 15 (13) (2023) 3337.

[12] J.Y. Liu, Space-based large spinning sensor pointing and control design and its application to NASA's SMAP spacecraft, in: AIAA Guidance, Navigation, and Control Conference, 2014, p. 1304.

[13] P. Iannelli, F. Angeletti, P. Gasbarri, A model predictive control for attitude stabilization and spin control of a spacecraft with a flexible rotating payload, Acta Astronaut. 199 (2022) 401–411, http://dx.doi.org/10.1016/j.actaastro.2022.07.024.

[14] F. Wang, C. Wang, X. qin Chen, C. fei Yue, Y. fei Xie, L. peng Chai, High-precision control method for the satellite with large rotating components, Aerosp. Sci. Technol. 92 (2019) 91–98, http://dx.doi.org/10.1016/j.ast.2019.05.036, URL https://www.sciencedirect.com/science/article/pii/S1270963819300987.

[15] S. Meraglia, D. Invernizzi, M. Lovera, T. Mohtar, A. Bursi, Design of an active balancing system for rotating orbital devices, J. Guid. Control Dyn. 46 (12) (2023) 2315–2329, http://dx.doi.org/10.2514/1.G007385.

[16] D. Invernizzi, Modeling and attitude control of spacecraft with an unbalanced rotating device, IEEE Control. Syst. Lett. 7 (2023) 466–471, http://dx.doi.org/10.1109/LCSYS.2022.3187877.

[17] X. Zhao, Y. Geng, C. Yuan, B. Wu, An unscented Kalman filter–based iterative learning controller for multibody rotating scan optical spacecraft, Trans. Inst. Meas. Control 44 (12) (2022) 2418–2433, http://dx.doi.org/10.1177/01423312221085268.

[18] J. Fisher, S.R. Vadali, Gyroless attitude control of multi-body satellites using an unscented Kalman filter, in: AIAA/AAS Astrodynamics Specialist Conference and Exhibit, Vol. 31, American Institute of Aeronautics and Astronautics, 2006, pp. 245–251.

[19] J. Fisher, S.R. Vadali, Gyroless attitude control of multibody satellites using an unscented Kalman filter, J. Guid. Control Dyn. 31 (1) (2008) 245–251.

[20] F.E. Scarsi, A. Battaglia, F. Tridon, P. Martire, R. Dhillon, A. Illingworth, Mispointing characterization and Doppler velocity correction for the conically scanning WIVERN Doppler radar, Atm. Meas. Tech. 17 (2) (2024) 499–514, http://dx.doi.org/10.5194/amt-17-499-2024, URL https://amt.copernicus.org/articles/17/499/2024/.

[21] P.C. Hughes, Spacecraft Attitude Dynamics, Dover Publications, 2004.

[22] R.E. Roberson, R. Schwertassek, Dynamics of Multibody Systems, Springer Berlin, Heidelberg, 1988, http://dx.doi.org/10.1007/978-3-642-86464-3.

[23] J. Alcorn, C. Allard, H. Schaub, Fully coupled reaction wheel static and dynamic imbalance for spacecraft Jitter modeling, J. Guid. Control Dyn. 41 (6) (2018) 1380–1388, http://dx.doi.org/10.2514/1.G003277.

[24] F. Manconi, A. Battaglia, P. Kollias, Characterization of surface clutter signal in presence of orography for a spaceborne conically scanning W-band Doppler radar (preprint), Atm. Meas. Tech. Disc. (2024) http://dx.doi.org/10.5194/egusphere-2024-2779.

[25] A. Bani Younes, D. Mortari, Derivation of all attitude error governing equations for attitude filtering and control, Sensors 19 (21) (2019) http://dx.doi.org/10.3390/s19214682.

[26] P. Zarchan, H. Musoff, Fundamentals of Kalman Filtering: A Practical Approach, vol. 232, American Institute of Aeronautics and Astronautics, 2009.

[27] E. Canuto, C. Novara, D. Carlucci, C.P. Montenegro, L. Massotti, Spacecraft Dynamics and Control: the Embedded Model Control Approach, Butterworth-Heinemann, 2018.

[28] IEEE, Standard Specification Format Guide and Test Procedure for Single-Axis Interferometric Fiber Optic Gyros, IEEE Std 952- 1997, 1998, pp. 1–84, http://dx.doi.org/10.1109/IEEESTD.1998.86153.

[29] ESA-ESTEC requirements & standards division, ECSS-E-ST-60-21C, gyro terminology and performance specification, 2017.

[30] O.J. Woodman, An Introduction to Inertial Navigation, Tech. Rep., University of Cambridge, Computer Laboratory, 2007, URL https://www.cl.cam.ac.uk/techreports/UCAM-CL-TR-696.pdf.

[31] S. Airbus, Astrix® 200 fiber optic gyroscope, 2022, URL https://www.airbus.com/sites/g/files/jlcbta136/files/2022-02/ScE-AVIONICS-ASTRIX120v3_2022.pdf.

[32] A. Ellin, G. Dolsak, The design and application of rotary encoders, Sensor Rev. 28 (2) (2008) 150–158.

[33] H.-K. Jia, L.-D. Yu, H.-N. Zhao, Y.-Z. Jiang, A new method of angle measurement error analysis of rotary encoders, Appl. Sci. 9 (16) (2019) 3415.

[34] H. Wang, J. Wang, B. Chen, P. Xiao, X. Chen, N. Cai, B.W.-K. Ling, Absolute optical imaging position encoder, Meas. 67 (2015) 42–50.

[35] M. Reinhardt, K. Panzlaff, K.-G. Friederich, F. Heine, R. Himmler, K. Maier, E. Mössl, C. Parker, S. McAdam, J. Slack, R. Meyer, High precision encoders for GEO space applications, in: Proceedings International Conference on Space Optical Systems and Applications (ICSOS) 2012, 2012, pp. 8–1.

[36] Renishaw encoder division, the accuracy of rotary encoders, 2019, URL https://www.renishaw.com/media/pdf/en/e429717c39ca479b8860c69e15fadf6a.pdf.

[37] BEI Precision, BEI precision nanoseries® housed nSH/80 encoder datasheet, 2019, URL https://www.quanticbei.com/wp-content/uploads/2019/08/MM-261-Rev-A-nSH80-data-sheet.pdf.

[38] M.J. Sidi, Spacecraft Dynamics and Control: a Practical Engineering Approach, vol. 7, Cambridge University Press, 1997.

[39] C. Siemes, M. Rexer, R. Haagmans, GOCE star tracker attitude quaternion calibration and combination, Adv. Space Res. 63 (3) (2019) 1133–1146.

[40] T. Bandikova, J. Flury, Improvement of the GRACE star camera data based on the revision of the combination method, Adv. Space Res. 54 (9) (2014) 1818–1827.

[41] L.J. Romans, Optimal combination of quaternions from multiple star cameras, JPL Interoffice Memo. (2003) URL https://archive.podaac.earthdata.nasa.gov/podaac-ops-cumulus-docs/grace/open/docs/quaternion_memo.pdf.

[42] ESA-ESTEC requirements & standards division, ECSS-E-ST-60-20C rev.2, star sensor terminology and performance specification, 2019.

[43] S. Winkler, G. Wiedermann, W. Gockel, High-accuracy on-board attitude estimation for the GMES sentinel-2 satellite: concept, design, and first results, in: AIAA Guidance, Navigation and Control Conference and Exhibit, 2008, p. 7482.

[44] A. Gelb, et al., Applied Optimal Estimation, MIT Press, 1974.

[45] Sodern, Hydra multiple head star tracker with high performance, 2021, URL https://sodern.com/wp-content/uploads/2021/11/Hydra.pdf.

[46] On semiconductor, NOIH2SM1000A HAS2 image sensor, 2015, Rev. 14.

[47] ESA-ESTEC requirements & standards division, ECSS-E-HB-60-10A, control performance guidelines, 2010.

[48] Constellation Series Reaction Wheels, Honeywell International Inc., 2003, URL https://www.satcatalog.com/component/hr14-50/.

Francesco Manconi graduated in Aerospace Engineering from Politecnico di Torino in 2022. Over the course of two years as a research fellow, he worked on Guidance, Navigation, and Control for CubeSats and larger spacecraft. He is currently pursuing a Ph.D. in Aerospace Engineering at Politecnico di Torino, focusing on simulation and pointing correction for spaceborne radar missions. He has been involved in a variety of projects and is currently working on ESA's WIVERN and ESA/JAXA's EarthCARE missions.

Paolo Martire received a B.Sc. and a M.Sc. in Aerospace Engineering from Politecnico di Torino in 2019 and 2021. He is currently pursuing a Ph.D. program in Aerospace Engineering at Politecnico di Torino, focusing on spacecraft attitude guidance, dynamics and control. Paolo has been involved with ESA's WIVERN and NASA's INCUS missions, working on solutions for spaceborne radar pointing. He is currently conducting research at NASA's Jet Propulsion Laboratory as a Ph.D. visiting student.

Fabrizio Stesina is Assistant Professor in Aerospace Systems Engineering at Politecnico di Torino, Systems Engineer of CubeSat missions developed at PoliTO, and Facility Manager of the Systems and Technology for Aerospace Research (STAR) laboratory. He has a strong expertise in Guidance, Navigation and Control Systems and Algorithms, Advanced Simulation (Real-time Hardware-in-the-loop simulation), and Verification & Testing processes. He has participated in several international research projects within EC, ESA, and the space industry.

Alessandro Battaglia graduated at the University of Padova, Italy, with a thesis in Particle Physics and received the Ph.D. degree in Physics at the University of Ferrara, Italy. He is experienced in microwave remote sensing of clouds and precipitation with a specific interest in spaceborne radars. He is Associate Professor at Politecnico di Torino, Turin, Italy. He is a member of the NASA Precipitation Measuring Mission Science Team and of the INCUS Team, a member of the ESA MAG of EarthCARE and WIVERN, and an author or co-author of more than 140 peer-reviewed journal papers.